AIAA 2001-0634

Application of Combined LES and Flamelet Modeling to Methane, Propane, and Jet-A Combustion

Foluso Ladeinde & Xiaodan Cai
Aerospace Research Corp., L.I.
Stony Brook, L.I., New York 11790

Balu Sekar & Barry Kiel
Aero-Propulsion and Power Directorate, AFRL
Wright-Patterson AFB, OH 45433-7251

39th AIAA Aerospace Sciences Meeting & Exhibit
8-11 January 2001 / Reno, NV

Application of Combined LES and Flamelet Modeling to Methane, Propane, and Jet-A Combustion

Foluso Ladeinde*and **Xiaodan Cai**†
Aerospace Research Corp., L.I.
25 East Loop Road,
Stony Brook, NY 11790-0609

Balu Sekar‡and **Barry Kiel**§
Aero-Propulsion and Power Directorate
Air Force Research Laboratory
Wright-Patterson AFB, OH 45433-7251

Abstract

This paper reports on the performance of the flamelet model for diffusion flames when combined with the Large Eddy Simulation (LES) and assumed probability density functions for the mixture fraction and its dissipation rate. The flamelet equations are reduced to a set of first order ordinary differential equations and calculated very cheaply using Newton's iteration. The LES models support both the standard Smagorinsky and the dynamic approaches and are numerically calculated using the sixth-order compact diffusing and tenth-order filtering schemes. Time integration is done with the standard fourth-order Runge-Kutta procedure. The effects of three models for the probability density function of the mixture fraction are discussed. Also presented are various assumptions for the stoichiometric value of the mixture fraction dissipation rate and the effect on the combustion simulation results. The application of the developed procedures to the combustion of methane/air, propane/air, jet-A/air, and hydrogen/air are reported. In the case of methane, the performance for homogeneous turbulence and spatially-evolving mixing layers are also reported.

*Senior Member, AIAA; Director of Research
†Member, AIAA; Senior Research Engineer
‡Research Aerospace Engineer
§R & D Program Manager

1 Introduction

In comparison to the Reynolds-averaged Navier-Stokes (RANS) method, the Large Eddy Simulation (LES) method of calculating turbulent flows offers more advantages. RANS models rely heavily on empirically adjusted constants and hence vary significantly from problem to problem. In LES[1,2,3], the motions of the large eddies are simulated so that only the small scales of turbulence need to be modeled. Because these small eddies contain only a small portion of the total kinetic energy, the computed flows are usually less sensitive to the turbulence modeling. Also, the small eddies tend to be more universal in character, so that LES models could be valid for a wide range of problems.

Until recently, LES has not been applied to combustion. Unlike the hydrodynamic part of a reacting flow, where the small scales do not have the controlling influence, reactions typically take place within diffusion zones that are too thin to be resolved by an LES grid, suggesting the need to model the entire reaction. To avoid this daunting task, Gao and O'Brien[4] accounted for subgrid scale mixing by assuming the form of the probability density function (PDF) of a scalar variable within a cell volume, leading to a procedure they termed "large eddy probability density function (LEPDF)." The procedure has been shown to be accurate for equilibrium chemistry[5]. Frankel et al.[6]showed

that it could be used for LES of non-premixed, turbulent, reacting flows with both equilibrium and finite rate chemistry. For the non-equilibrium chemistry case, they employed the joint β distribution for the fuel and oxidizer in a flow with single-step chemistry.

Subgrid scale modeling of premixed combustion has been studied by Menon and his co-workers[7,8,10]. Colucci et al.[11] developed a subgrid scale methodology termed "filtered density function" or FDF, for short. In this case, the effects of subgrid scale fluctuations are accounted for in a probabilistic manner, which, incidentally, is conceptually very similar to LEPDF. This procedure was extended to three-dimensional turbulent reacting jet flow by Garrick et al.[12].

The present work uses the flamelet[13] procedure in conjunction with the LES method to model turbulent diffusion flames. Our interest in the flamelet approach stems from the ability of the procedure to cheaply compute very complex reactions, including detailed mechanisms. Note, however, that the flamelet procedure by Peters is normally employed within the framework of RANS, using the $k-\varepsilon$ turbulence model and the KIVA code. The limitations of the RANS procedure have been mentioned above.

The basic development of the LES-flamelet approach used for diffusion flames in the present paper is contained in the paper by Cook and Riley[14]. However, the present work uses this technique within the framework of the high-order Padé-type compact schemes[15] and the high-order filter schemes. This numerical scheme, without combustion and turbulence, has been proposed for, and applied[16] to, aeroacoustic computations, which requires very high accuracy and low dispersion errors. Thus, the procedure in the present paper is well suited to the prediction of combustion aeroacoustic instability. Another improvement of our work over [14] is the use of a generalized curvilinear coordinate system to permit the calculation of turbulent combustion in realistic systems, which usually have complex geometries. Finally, the present work presents results for fairly complicated, but interesting reactions involving methane (see also [17]), propane, and Jet-A fuels. The evaluation of the accuracy of the predictions is done at two levels. For the LES modeling, we compare the resolved turbulence energy to DNS results for the canonical problem of homogeneous turbulence, while the flamelet calculations are evaluated by comparing the result for methane/air from three mechanisms. Although a great deal of results has been obtained and evaluated, only a few representative samples are presented in this paper.

2 Kinetic Mechanisms

The mechanisms analyzed in the present work are as follows: Propane/Air, Jet-A/Air, Hydrogen/Air, and three mechanisms for Methane/Air.

2.1 Mechanisms for Propane/Jet-A

The mechanisms for Propane/Jet-A involve 16 species and 23 steps. The various reaction steps are shown in the table below, along with the Arrhenius constants in

$$k = AT^n \exp\left(-\frac{E}{RT}\right)[X]^a[Y]^b[G]^c,$$

where A is the frequency factor, with the unit cm-sec-mole-cal-Kelvin), n is the pre-exponential temperature exponent, E is the activation energy with the units of cal/mole, and R is the universal gas constant, = 8.3147 J/mole·K. Each reaction in the table has its own values for A, n, and E. Unless otherwise specified, a, b, and c in the table are the stoichiometric coefficients: aX + gY +cG. The symbols "f" and "b" in reactions 2, 3, and 5 imply forward and backward reactions, respectively.

Table 1: Reaction Steps and the Arrhenius Constants for the Full Mechanism

1.1 Global Reaction for Propane:

Nr.	Reaction
1-P	$\{N_2\} + C_3H_8 \longrightarrow 3CH + 5H + \{N_2\}$

1.2 Global Reaction for Jet-A:

1-J	$\{N_2\} + C_{12}H_{23} \longrightarrow 12CH + 11H + \{N_2\}$
	a=0.8, b=0.8

1.3 Global Reactions Common to Propane and Jet-A:

2f	$\{CH\} + H_2 + N_2 \longrightarrow 2NH + \{CH\}$
	a=2.0, b=0.1, c=1.0
2b	$\{CH\} + NH \longrightarrow N_2 + H_2 + \{CH\}$
	a=1.0, b=2.0
3f	$\{O\} + N_2 + HO_2 \longrightarrow 2NO + H + \{O\}$
	a=1.0, b=0.5, c=1.0
3b	$2NO + H \longrightarrow N_2 + HO_2$
	a=1.0, b=1.0
4	$\{N_2\}\ CO + HO_2 \longrightarrow CO_2 + OH + \{N_2\}$
5f	$\{H_2\} + 2O \longrightarrow 2O + \{N_2\}$
	a=1.0, b=1.0
5b	$\{H_2\} + 2O \longrightarrow O_2 + \{H_2\}$
	a=1.0, b=2.0

1.4 Kinetic Reactions Common to Propane and Jet-A:

Nr.	Reaction
6.	$H_2 + OH \longrightarrow H_2O + H$
7.	$H_2 + O \longrightarrow H + OH$
8.	$H + O_2 \longrightarrow O + OH$
9.	$H_2 + 2H \longrightarrow 2H_2$
10.	$H + O_2 \longrightarrow HO_2$
11.	$H + HO_2 \longrightarrow H_2 + O_2$
12.	$H + HO_2 \longrightarrow OH + O_2$
13.	$CO + OH \longrightarrow CO_2 + H$

Nr.	Reaction
14.	$\{N_2\} + 2CH \longrightarrow C_2H_2 + \{N_2\}$
15.	$C_2H_2 + O_2 \longrightarrow 2CO + H_2$
16	$CH + O \longrightarrow CO + H$
17.	$CH + OH \longrightarrow CO + H_2$
18.	$CH + NO \longrightarrow NH + CO$
19.	$N_2 + O \longrightarrow N + NO$
20.	$N + O_2 \longrightarrow NO + O$
21.	$NO + H \longrightarrow N + OH$
22	$NH + O \longrightarrow NO + H$
23.	$NH + NO \longrightarrow N_2 + OH$

Nr.	A	n	E
1-P	4.50E+10	0.0	30,000.00
1-J	5.50E+10	0.0	30,000.00
2f	1.00E+16	0.0	78000.00
2b	1.95E+15	0.00	53,900.00
3f	1.95E+15	0.00	41,900.00
3b	1.25E+10	0.00	6,000.00
4	3.50E+13	0.00	22,934.00
5f	1.00E+18	0.00	122,239.00
5b	1.00E+18	0.00	0.00

Nr.	A	n	E
6.	1.17E+11	1.30	3,626.00
7.	2.50E+15	0.00	6,000.00
8.	4.00E+14	0.00	18,000.00
9.	4.00E+20	-1.00	0.00
10.	1.00E+15	-.87	0.00
11.	1.50E+14	0.00	0.00
12.	2.50E+15	0.00	0.00
13.	1.51E+07	1.30	-758.00
14.	1.00E+18	0.00	-758.00
15.	3.00E+16	0.00	19,000.00
16	1.00E+12	0.70	0.00
17.	1.00E+13	0.00	0.00
18.	1.00E+11	0.00	0.00
19.	9.00E+13	0.00	75,000.00
20.	6.30E+09	1.00	6,300.00
21.	1.00E+12	0.00	0.00
22	2.50E+04	2.64	0.00
23.	2.00E+15	-0.80	0.00

2.2 Three mechanisms for Methane/Air

Mechanism 1: This model involves the oxidation of a Methane/Nitrogen mixture by an Oxygen/Nitrogen mixture, with the three reactions

$$Fuel + Oxi \rightarrow Int + Prod, \qquad \text{(I)}$$

$$Int + Oxi \rightarrow 2Prod, \qquad \text{(II)}$$

$$N_2 + Oxi \rightarrow 2NO, \qquad \text{(III)}$$

where *Fuel* is CH_4, *Oxi* is O_2, *Int* is $(\frac{4}{3}H_2 + \frac{2}{3}CO)$, and *Prod* is $(\frac{2}{3}H_2O + \frac{1}{3}CO_2)$. Reactions I and II represent the oxidation of methane while the third reaction represents the formation of nitric oxide. The fuel stream consists of 15% methane (by mass), balance nitrogen; the oxidizer stream consists of 30% oxygen,

balance nitrogen. Therefore, the steady flamelet equations are

$$a\frac{d^2Y_O}{dZ^2} - \left(\dot{\omega}_I + \dot{\omega}_{II}\right)\cdot\frac{M_O}{\rho} = 0, Y_O(Z=0) = 0.30,$$

$$Y_O(Z=1) = 0$$

$$a\frac{d^2Y_F}{dZ^2} - \dot{\omega}_I\cdot\frac{M_{CH4}}{\rho} = 0, \qquad Y_F(Z=0) = 0,$$

$$Y_A(Z=1) = 0.15;$$

$$a\frac{d^2Y_O}{dZ^2} - \left(\dot{\omega}_I + \dot{\omega}_{II}\right)\cdot\frac{M_O}{\rho} = 0, \qquad Y_O(Z=0) = 0.30,$$

$$Y_O(Z=1) = 0;$$

$$a\frac{d^2Y_I}{dZ^2} + \left(\dot{\omega}_I - \dot{\omega}_{II}\right)\cdot\frac{M_I}{\rho} = 0, \qquad Y_I(Z=0) = 0.0,$$

$$Y_I(Z=1) = 0;$$

$$a\frac{d^2Y_P}{dZ^2} + \left(\dot{\omega}_I + \dot{\omega}_{II}\right)\cdot\frac{M_P}{\rho} = 0 \qquad Y_P(Z=0) = 0,$$

$$Y_P(Z=1) = 0;$$

where $a = \frac{\rho}{2}\chi$, and

$$\dot{\omega}_I = 1375\cdot T^3\cdot e^{-4404/T}\,[Fuel]\,[H],$$

$$\dot{\omega}_{II} = 7.19\times 10^{16}\cdot T^{-0.8}\cdot[Oxi]\,[H]\,\Gamma_M.$$

In the above expressions, the units are *moles*, *cm*, *K*, *s*, and *Joules*. $[i]$ is the concentration of species i, which has a relation with the mass fraction Y_i as $[i] = \frac{Y_i}{M_i}\cdot\rho$, and

$$[H] = 0.136\cdot e^{3045/T}\cdot\Theta\cdot\left[1 - e^{-10^{-15}T^5}\right]\cdot\frac{\left([Oxi]\,[Int]^3\right)^{1/2}}{[\mathrm{Pr}\,od]},$$

$$\Theta = \exp\left\{-4.26\times 10^{-10}T^3\frac{[Fuel]}{[Oxi]}\cdot e^{4051/T}\right\},$$

$$\Gamma_M = 0.014 + 0.392Y_F - 0.002Y_O + 0.072Y_I + 0.167Y_P.$$

It has a flame-sheet solution as described in Eqs. (3)-(12) below, where $T_1 = T_2 = 300K$, $Y_{F,1} = 0.15$, $Y_{O,2} = 0.30$, and $Z_{st} = \frac{1}{3}$. We also have $M_F = 16$, $\nu_F = 1$; $M_O = 32$, $\nu_O = 2$; and $M_P = \frac{80}{3}$, $\nu_P = 3$ for the above flame-sheet evaluation. However, the flame-sheet solution only provides a guess for the major species, and the reaction cannot be started without the information from the intermediate product, *Int*. Therefore, an adjustable Gaussian profile, which is centered in the reaction zone and has peak values of at most a few percent, is provided to estimate the initial distribution of Y_I. The heat release, Q, has the value of

$$Q = \frac{Q_I + Q_{II}}{C_P\cdot M_F\nu_F},$$

where $Q_I = 2.91\times 10^5\left(J\cdot mol^{-1}\right)$, $Q_{II} = 5.11\times 10^5\left(J\cdot mol^{-1}\right)$, and $C_P = 1.30\left(J\cdot g^{-1}\cdot K^{-1}\right)$. Figs. 1 through 5 show the distributions of the mass fractions of *Fuel*, *Oxi*, *Int* and *Prod* in the mixture-fraction space, which is consistent with the DNS results obtained in Bushe et al[20].

Mechanism 2: In this reduced mechanism, steady state approximations are used for the species CH_3, CH_2, CH, CH_2O, HCO, OH, O, HO_2, and H_2O_2, leading to a four-step/seven-species mechanism from the starting mechanism (i.e., the full mechanism below):

$CH_4+2H+H_2O \rightleftharpoons CO+4H_2,$	I
$CO+H_2O \rightleftharpoons CO_2+H_2,$	II
$H+H+M' \rightleftharpoons H_2,$	III
$O_2+3H_2 \rightleftharpoons 2H+2H_2O,$	IV

The reaction rates for the overall steps in I through IV can be expressed in terms of the elementary rates from the starting mechanism: $\omega_I = -\omega_{34}+\omega_{38}+\omega_{39}+\omega_{40}$,

$$\omega_{II} = \omega_{18} - \omega_{20} + \omega_{28},$$

$$\omega_{III} = \omega_5 + \omega_{12} + \omega_{15} + \omega_{16} + \omega_{17} + \omega_{21} + \omega_{22} + \omega_{23} - \omega_{32} + \omega_{34},$$

$$\omega_{IV} = \omega_1 + \omega_6 + \omega_9 - \omega_{12} + \omega_{13} - \omega_{17} - \omega_{20} + \omega_{27} + \omega_{28} + \omega_{37}.$$

The species that appear in the starting mechanism but not in the reduced mechanism are calculated as follows. Following [21], the value of [OH] is obtained under the assumption that reaction 3 in the starting mechanism is in partial equilibrium, leading to

$$[\mathrm{OH}] = \frac{k_{3b}[\mathrm{H_2O}][\mathrm{H}]}{k_{3f}[\mathrm{H_2}]}.$$

The approximation could introduce changes to the representation of the overall reduced mechanism but the changes were found to have negligible effects on

extinction predictions. Note that the right-hand-side of this equation comes directly from the solution of the 4-step mechanism. The steady state concentrations of CH_2, CH, O, CH_2O, CHO, HO_2, and H_2O_2 can then be obtained from the reduced mechanism results as follows:

$$[CH_2] = \frac{k_{33}[CH_3]}{k_{25f}[H]+(k_{27f}+k_{28f})[O_2]},$$

$$[CH] = \frac{k_{25f}[H][CH_2]}{k_{19f}[O_2]+k_{20f}[CO_2]},$$

$$A = k_{4f}[OH]^2+k_{19}[CH][O_2],$$

$$B = k_{26f}[CH_2]+k_{35f}[CH_3]+k_{38f}[CH_4]$$

$$[O] = \frac{k_{1f}[O_2][H]+k_{2b}[OH][H]\}+ A}{k_{1b}[OH]+k_{2f}[H_2]+k_{4b}[H_2O]+ B},$$

$$[CH_2O] = \frac{(k_{35f}[O]+k_{37f}[O_2]\ )[CH_3]}{k_{29f}[H]+k_{30f}[O]+k_{31f}[OH]+k_{32f}[M]},$$

$$[HCO] = \frac{(\ k_{29f}[H]+k_{31f}[OH]\ )[CH_2O] + (k_{19f}[O_2]+k_{20f}[O_2]\ )\ [CH]}{k_{21f}[H]+k_{22f}[OH]+k_{23f}[O_2]+k_{24f}[M]},$$

$$[HO_2] = \frac{k_{5f}[H][O_2][M]+k_{23f}[HCO][O_2]}{(\ k_{26f}+k_{7f}+k_{9f}\ )\ [H]\ +\ k_{8f}[OH]+k_{10f}[O]}$$

$$[H_2O_2] = \frac{(\ k_{11f}[HO_2]+k_{14b}[H_2O]\ )\ [HO_2]+k_{12f}[OH]^2[M]}{k_{12b}[M]+k_{13f}[H]+k_{14f}[OH]}.$$

Note that, in order to arrive at the expressions above, the influences of some of the reactions have been neglected [23]. The molar concentration of oxygen, [O], can be calculated as

$$[O] = \frac{\beta+\sqrt{\beta^2+4\alpha\gamma}}{2\alpha},$$

where

$$\alpha = k_{35f}(k_{1bf}[OH]\ +\ k_{2f}[H_2]\ +\ k_{4b}[H_2O],$$

$$\beta = (\ k_{1b}[OH]\ +\ k_{2f}[H_2]\ +\ k_{4b}\ [H_2O]\ )$$
$$+(\ k_{1b}(\ k_{34f}[H]\ +\ k_{38b}[H_2]+\ k_{40b}[H_2O]+k_{33f}[H]\ )$$
$$+\ k_{35f}\{k_{1f}[H][O_2]+k_{2b}[OH][H]+k_{4f}[OH]^2\ -$$
$$(\ k_{38f}[H]+k_{40f}[OH]\ )\ [CH_4]\ \},$$

$$\gamma = (\ k_{1f}[H][O_2]+k_{2b}[OH][H]+k_{4f}[OH]^2\ )\ (\ k_{34f}[H]+k_{38b}[H_2]$$
$$+k_{40b}[H_2O]+k_{33f}[H]\ ).$$

Full Mechanism: This is a detailed kinetics model for CH_4/Air that was compiled from several sources by Peters. The various reaction steps are shown in the table below, along with the Arrhenius constants in

$$k = AT^n \exp\left(-\frac{E}{RT}\right),$$

where A is the frequency factor, n is the pre-exponential temperature exponent, E is the activation energy, and R is the universal gas constant, = 8.3147 J/mole.K. Each reaction in the table has its own values for A, n, and E.

Table 2: Reaction Steps and the Arrhenius Constants for the Full Mechanism

1.1 H_2/O_2 Chain Reactions

Nr.	Reaction	A	n	E
1f	$O_2+H \longrightarrow OH+O$	2.000E+14	0.00	70.30
1b	$OH+O \longrightarrow O_2+H$	1.568E+13	0.00	3.52
2f	$H_2+O \longrightarrow OH+H$	5.060E+04	2.67	26.30
2b	$OH+H \longrightarrow H_2+O$	2.222E+04	2.67	18.29
3f	$H_2+OH \longrightarrow H_2O+H$	1.000E+08	1.60	13.80
3b	$H_2O+H \longrightarrow H_2+OH$	4.312E+08	1.60	76.46
4f	$OH+OH \longrightarrow H_2O+O$	1.500E+09	1.14	0.42
4b	$H_2O+O \longrightarrow OH+OH$	1.473E+10	1.14	71.09

1.2 HO_2 Formation and Consumption

Nr.	Reaction
5f	$O_2+H+M' \longrightarrow H_2O+M'$
5b	$HO_2 + M' \longrightarrow O_2+H+M'$
6	$HO_2+H \longrightarrow OH+OH$
7	$HO_2+H \longrightarrow H_2+O_2$
8	$H_2O+OH \longrightarrow H_2O+O_2$
9	$HO_2+H \longrightarrow H_2O+O$
10	$H_2O+O \longrightarrow OH+O_2$

Nr.	A	n	E
5f	2.300E+18	-0.80	0.00
5b	3.190E+18	-0.80	195.39
6	1.500E+14	0.00	4.20
7	2.500E+13	0.00	2.90
8	6.000E+13	0.00	0.00
9	3.000E+13	0.00	7.20
10	1.800E+13	0.00	-1.70

1.3 H_2O_2 Formation and Consumption

Nr.	Reaction
11	$HO_2+HO_2 \longrightarrow H_2O_2+O_2$
12	$OH+OH+M' \longrightarrow H_2O_2+M'$
12b	$H_2O_2+M' \longrightarrow OH+OH+M'$
13	$H_2O_2+H \longrightarrow H_2O+OH$
14f	$H_2O_2+OH \longrightarrow H_2O+HO_2$
14b	$H_2O+HO_2 \longrightarrow H_2O_2+OH$

Nr.	A	n	E
11	2.500E+11	0.00	-5.20
12	3.250E+22	-2.00	0.00
12b	1.692E+24	-2.00	202.29
13	1.000E+13	0.00	15.00
14f	5.400E+12	0.00	4.20
14b	1.802E+12	0.00	134.75

1.4 Recombination Reactions

Nr.	Reaction
15	$H+H+M' \longrightarrow H_2+M'$
16	$OH+H+M' \longrightarrow H_2O+M'$
17	$O+O+M' \longrightarrow O_2+M'$

Nr.	A	n	E
15	1.800E+18	-1.00	0.00
16	2.200E+22	-2.00	0.00
17	2.900E+17	-1.00	0.00

2. CO/CO_2 Mechanism

Nr.	Reaction
18f	$CO+OH \longrightarrow CO_2+H$
18b	$CO_2+H \longrightarrow CO+OH$

Nr.	A	n	E
18f	4.400E+06	1.50	-3.10
18b	4.956E+08	1.50	89.76

3.1 CH Consumption

Nr.	Reaction	A	n	E
19	$CH+O_2 \longrightarrow CHO+O$	3.000E+13	0.00	0.00
20	$CO_2+CH \longrightarrow CHO+CO$	3.400E+12	0.00	0.00

3.2 CHO Consumption

Nr.	Reaction
21	$CHO+H \longrightarrow CO+H_2$
22	$CHO+OH \longrightarrow CO+H_2O$
23	$CHO+O_2 \longrightarrow CO+HO_2$
24f	$CHO+M' \longrightarrow CO+H+M'$
24b	$CO+H+M' \longrightarrow CHO+M'$

Nr.	A	n	E
21	2.000E+14	0.00	0.00
22	1.000E+14	0.0	0.0
23	3.000E+12	0.00	0.00
24f	7.100E+14	0.00	70.30
24b	1.136E+15	0.00	9.97

3.3 CH_2 Consumption

Nr.	Reaction
25f	$CH_2+H \longrightarrow CH+H_2$
25b	$CH+H_2 \longrightarrow CH_2+H$
26	$CH_2+O \longrightarrow CO+H+H$
27	$CH_2+O_2 \longrightarrow CO+OH+H$
28	$CH_2+O_2 \longrightarrow CO_2+H+H$

Nr.	A	n	E
25f	8.400E+09	1.50	1.40
25b	5.830E+09	1.50	13.08
26	8.000E13	0.00	0.00
27	6.500E+12	0.00	6.30
28	6.500E+12	0.00	6.30

3.4 CH_2O Consumption

Nr.	Reaction
29	$CH_2O+H \longrightarrow CHO+H_2$
30	$CH_2O+O \longrightarrow CHO+OH$
31	$CH_2O+OH \longrightarrow CHO+H_2O$
32	$CH_2O+M' \longrightarrow CHO+H+M'$

Nr.	A	n	E
29	2.500E+13	0.00	16.70
30	3.500E+13	0.00	14.60
31	3.000E+13	0.00	5.00
32	1.4700E+17	0.00	320.00

3.5 CH_3 Consumption

Nr.	Reaction	
33f	$CH_3+H \longrightarrow CH_2+H_2$	
33b	$CH_2+H_2 \longrightarrow CH_3+H$	
34	$CH_3+H \longrightarrow CH_4$	k_∞
	$CH_3+H \longrightarrow CH_4$	k_0
35	$CH_3+O \longrightarrow CH_2O+H$	
36	$CH_3+CH_3 \longrightarrow C_2H_6$	k_∞
	$CH_3+CH_3 \longrightarrow C_2H_6$	k_0
37	$CH_3+O_2 \longrightarrow CH_2O+OH$	
38f	$CH_4+H \longrightarrow CH_3+H_2$	
38b	$CH_3+H_2 \longrightarrow CH_4+H$	
39	$CH_4+O \longrightarrow CH_3+OH$	
40f	$CH_4+OH \longrightarrow CH_3+H_2O$	
40b	$CH_3+H_2O \longrightarrow CH_4+OH$	

Nr.	A	n	E
33f	1.800E+14	0.00	63.00
33b	3.680E+13	0.00	44.30
34	2.108E+14	0.00	0.00
	6.257E+23	-1.80	0.00
35	7.000E+13	0.00	0.00
36	3.613E+13	0.00	0.00
	1.270E+41	-7.00	11.56
37	3.400E+11	0.00	37.40
38f	2.200E+04	3.00	36.60
38b	8.391E+02	3.00	34.56
39	1.200E+07	2.10	31.90
40f	1.600E+06	2.10	10.30
40b	2.631E+05	2.10	70.92

The rate coefficients for reactions 34 and 36 are calculated as a function of temperature and pressure:

$$k = F.k_\infty.k_L,$$

where

$$k_L = \frac{k_0[M]/k_\infty}{1 + k_0[M]/k_\infty},$$

$$\log_{10} F = \log_{10} F_c \frac{1}{1 + (\log_{10}[k_0[M]/k_\infty.1/N)^2},$$

$$N = 0.75 - 1.27 \log_{10} F_c$$

$$[M] = \sum_{i=1}^{n} \rho Y_i/M_i = p/RT$$

$$F_c = 0.577 \exp\left[-\frac{T}{2370.0}\right] \qquad \text{(Reaction 34)}$$

$$F_c = 0.38 \exp\left[-\frac{T}{73.0}\right] + 0.62 \exp\left[-\frac{T}{1180.0}\right] \qquad \text{(Reaction 36)}$$

Following [23], the present studies neglect Reaction 36.

2.3 Hydrogen/Air Mechanism

The mechanism used to test the applicability of the flamelet model to the hydrogen/air combustion was taken from the CHEMKIN III program and is presented in Table 3 below.

Table 3: Reaction Steps and the Arrhenius Constants for the Hydrogen/Air Mechanism

Nr.	Reaction
1	$H_2 + O_2 \rightleftharpoons 2OH$
2	$OH + H_2 \rightleftharpoons H_2O + H$
3	$O + OH \rightleftharpoons O_2 + H$
4	$O + H_2 \rightleftharpoons OH + H$
5	$H + O_2 + M \rightleftharpoons HO_2 + M$
	$H_2O/18.6/H_2/2.86/\ N_2/1.26/$
6	$OH + HO_2 \rightleftharpoons H_2O + O_2$
7	$H + HO_2 \rightleftharpoons 2OH$
8	$O + HO_2 \rightleftharpoons O_2 + OH$
9	$2OH \rightleftharpoons O + H_2O$
10	$H + H + M \rightleftharpoons H_2 + M$
	$H_2O/0.0/\ H_2/0.0/$
11	$H + H + H_2 \rightleftharpoons H_2 + H_2$
12	$H + H + H_2O \rightleftharpoons H_2 + H_2O$
13	$H + OH + M \rightleftharpoons H_2O + M$
	$H_2O/5/$
14	$H + O + M \rightleftharpoons O_2 + M$
	$H_2O/5/$
15	$O + O + M \rightleftharpoons O_2 + M$
16	$H + HO_2 \rightleftharpoons H_2 + O_2$
17	$HO_2 + HO_2 \rightleftharpoons H_2O_2 + O_2$
18	$H_2O_2 + M \rightleftharpoons OH + OH + M$
19	$H_2O_2 + H \rightleftharpoons HO_2 + H_2$
20	$H_2O_2 + OH \rightleftharpoons H_2O + HO_2$
21	$O + N_2 \rightleftharpoons NO + N$
22	$N + O_2 \rightleftharpoons NO + O$
23	$OH + N \rightleftharpoons NO + H$

Nr.	A	n	E
1	.170E+14	0.00	47780
2	.117E+10	1.30	3626
3	.400E+15	-0.50	0
4	.500E+05	2.67	6290
5	.361E+18	-0.72	0
6	.750E+13	0.00	0
7	.140E+15	0.00	1073
8	.140E+14	0.00	1073
9	.600E+19	1.30	0
10	.100E+19	-1.00	0
11	.920E+17	-0.60	0
12	.600E+20	-1.25	0
13	.160E+23	-2.0	0
14	.620E+17	-.60	0
15	.189E+14	0.00	-1788
16	.125E+14	0.00	0
17	.20E+13	0.00	0
18	.130E+18	0.00	45500
19	.160E+13	0.00	3800
20	.100E+14	0.00	1800
21	.140E+15	0.00	75800
22	.640E+10	1.00	6280
23	.400E+14	0.00	0

3 The Combined LES/Flamelet/ Assumed PDF Procedure

The procedural details for the flamelet/LES calculation of combustion are contained in Cook and Riley[9,14]. The essential steps in the present work are summarized. The LES procedure generates the filtered values of the standard dependent variables of the Navier-Stokes equation system plus the solution for the filtered mixture fraction at all grid points in the physical domain. Models are then invoked to compute the variance Z'' and dissipation rate χ of the mixture fraction Z. A "look-up" (interpolation) table for species mass fractions as a function of Z and χ is constructed by solving the flamelet equation for the mass fractions Y_i at discrete values of χ and Z. For this step, the range of Z is $0 \leq Z \leq 1$ while that of χ is pre-specified based on the combustion problem at hand, but are usually selected so that the flame is extinguished when the local value of the dissipation rate exceeds the maximum value in the look-up table. With infinite numbers of Z available via interpolation, the filtered value $\widetilde{Y}_i(x)$ can then obtained by integration with an assumed PDF. In this step, the value of χ at the specific x will be used for interpolation from the look-up table. The filtered mass fractions are then used to compute the filtered reaction rate that goes into the LES equations.

4 Subgrid Scale Modeling

The procedure used for subgrid scale modeling is presented in this section. The filtered continuity equation can be written as

$$\frac{\partial \overline{\rho}}{\partial t}+\frac{\partial}{\partial \xi}\left[\frac{\overline{\rho}U}{J}\right]+\frac{\partial}{\partial \eta}\left[\frac{\overline{\rho}V}{J}\right]+\frac{\partial}{\partial \zeta}\left[\frac{\overline{\rho}W}{J}\right]=0,$$

whereas the momentum equation in the ξ-direction is

$$\frac{\partial \overline{\rho}\widetilde{u}}{\partial t}+\frac{\partial}{\partial \xi}\left[\frac{\overline{\rho}\widetilde{u}U+\xi_x\overline{p}}{J}\right]+\frac{\partial}{\partial \eta}\left[\frac{\overline{\rho}\widetilde{u}V+\eta_x\overline{p}}{J}\right]+\frac{\partial}{\partial \zeta}\left[\frac{\overline{\rho}\widetilde{u}W+\zeta_x\overline{p}}{J}\right]$$
$$=\frac{1}{\mathrm{Re}}\left\{\left[\frac{\partial}{\partial \xi}\left(\frac{\xi_{x_i}\widetilde{\tau}_{i1}}{J}\right)\right]+\left[\frac{\partial}{\partial \eta}\left(\frac{\eta_{x_i}\widetilde{\tau}_{i1}}{J}\right)\right]+\left[\frac{\partial}{\partial \zeta}\left(\frac{\zeta_{x_i}\widetilde{\tau}_{i1}}{J}\right)\right]\right\}$$

where $\xi_{x_i}\widetilde{\tau}_{i1}$, $\eta_{x_i}\widetilde{\tau}_{i1}$, $\zeta_{x_i}\widetilde{\tau}_{i1}$ adopt standard tensor summation convention, $\widetilde{\tau}_{ij}$ is the subgrid turbulent Reynolds stress i.e.,

$$\widetilde{\tau}_{ij}=(\mu+\mu_T)\left\{\left(\frac{\partial \xi_k}{\partial x_j}\frac{\partial \widetilde{u}_i}{\partial \xi_k}+\frac{\partial \xi_k}{\partial x_i}\frac{\partial \widetilde{u}_j}{\partial \xi_k}\right)-\frac{2}{3}\delta_{ij}\frac{\partial \xi_k}{\partial x_l}\frac{\partial \widetilde{u}_l}{\partial \xi_k}\right\},$$

where

$$\mu_T=C_s^2\cdot\Delta^2\cdot|S|,|S|^2=2\widetilde{S}_{ij}\widetilde{S}_{ij},\Delta=\text{grid size};$$

C_s could be kept fixed (Smagorinsky) or obtained dynamically and locally using the dynamic LES method.

The momentum equations in the other two coordinate directions, η and ζ, take a similar form. The energy equation is

$$\frac{\partial}{\partial t}\left[\frac{\overline{\rho}\widetilde{E}_T}{J}\right]+\frac{\partial}{\partial \xi}\left[\frac{\overline{\rho}\widetilde{E}_TU+\overline{p}\overset{\vee}{U}}{J}\right]+\frac{\partial}{\partial \eta}\left[\frac{\overline{\rho}\widetilde{E}_TV+\overline{p}\overset{\vee}{V}}{J}\right]+\frac{\partial}{\partial \zeta}\left[\frac{\overline{\rho}\widetilde{E}_T\widetilde{W}+\overline{p}\overset{\vee}{W}}{J}\right]=$$
$$\frac{1}{\mathrm{Re}}\left[\frac{\partial}{\partial \xi}\left(\frac{\xi_{x_i}\widetilde{b}_i}{J}\right)+\frac{\partial}{\partial \eta}\left(\frac{\eta_{x_i}\widetilde{b}_i}{J}\right)+\frac{\partial}{\partial \zeta}\left(\frac{\zeta_{x_i}\widetilde{b}_i}{J}\right)\right]+\frac{1}{J}\left[\frac{1}{\gamma M_o^2}\cdot\sum_{i=1}^{N}h_i^o\overline{\dot{w}_i}\right],$$

where

$$\widetilde{E}_T=\widetilde{e}+\tfrac{1}{2}\widetilde{u}_i\widetilde{u}_i,$$
$$\widetilde{b}_i=\widetilde{u}_i\widetilde{\tau}_{ij}+\frac{\mu+\frac{\mathrm{Pr}\,\mu_T}{\mathrm{Pr}_T}}{\mathrm{Pr}\,(\gamma-1)\,M_o^2}\cdot\frac{\partial \xi_k}{\partial x_l}\cdot\frac{\partial \widetilde{T}}{\partial \xi_k},$$
$$f(Z)=\text{ PDF of mixture fraction,}$$
$$f(\chi_s)=\text{PDF of dissipation rate of } Z \text{ at } Z=Z_{st},$$
and $h_i^o=$ enthalpy of i^{th} species (standard formulation).

The filtered mixture fraction and reaction rate are obtained as follows:

$$\widetilde{Y}_i(z,t)=\int_0^1 Y_i(Z,x,t)\,\widetilde{p}(Z,x,t)\,dZ$$

$$\overline{\dot{w}_i}=\int\int \dot{w}_i(Da,Y_F,Y_o;Z,\chi_s)\cdot f(Z)\cdot f(\chi_s)\,dZd\chi_s.$$

Note that we have assumed that the joint PDF could be decomposed into a product of 2 PDFs. The equation of state is

$$T=\gamma M_o^2\cdot\frac{p}{\rho},$$

while Sutherland's viscosity law is assumed.

The general velocity is

$$U=\xi_x\widetilde{u}+\xi_y\widetilde{v}+\xi_z\widetilde{w}+\xi_t=\overset{\vee}{U}+\xi_t.$$

The equation for the filtered mixture fraction is also solved during the LES step of the procedure:

$$\frac{\partial}{\partial t}\left[\frac{\overline{\rho}\widetilde{Z}}{J}\right]+\frac{\partial}{\partial \xi}\left[\frac{\overline{\rho}\widetilde{Z}\widetilde{U}}{J}\right]+\frac{\partial}{\partial \eta}\left[\frac{\overline{\rho}\widetilde{Z}\widetilde{V}}{J}\right]+\frac{\partial}{\partial \zeta}\left[\frac{\overline{\rho}\widetilde{Z}\widetilde{W}}{J}\right]$$
$$=\frac{1}{\mathrm{Re}}\left[\frac{\partial}{\partial \xi}\left(\frac{\xi_{x_i}\widehat{a}_i}{J}\right)+\frac{\partial}{\partial \eta}\left(\frac{\eta_{x_i}\widehat{a}_i}{J}\right)+\frac{\partial}{\partial \zeta}\left(\frac{\zeta_{x_i}\widehat{a}_i}{J}\right)\right],$$

where

$$\widehat{a}_i=\left(\frac{\mu}{Sc}+\frac{\mu}{Sc_t}\right)\cdot\frac{\partial \xi_l}{\partial x_i}\cdot\frac{\partial \widetilde{Z}}{\partial \xi_l}.$$

The variance of the mixture fraction is modeled as:

$$Z''^2=\overline{Z^2}-\left(\overline{Z}^2\right)\approx C_s\left[\widetilde{\overline{Z}^2}-\left(\widetilde{\overline{Z}}\right)^2\right],$$

whereas its dissipation rate is modeled as

$$\overline{\chi}=C_d\cdot\widetilde{\rho}D\left(\widetilde{T}\right)\cdot\frac{\partial \widetilde{Z}}{\partial \chi_i}\cdot\frac{\partial \widetilde{Z}}{\partial \chi_i}.$$

The PDFs are assumed to take the forms

$$f(Z) = \frac{Z^{a-1}(1-Z)^{b-1}}{B(a,b)} : \beta - \text{PDF form}$$

$$\text{and } f(\chi_s) = \delta(\overline{\chi}) : \delta - \text{function.}$$

5 Solution of the Flamelet Equations

The unfiltered form of the flamelet equations is used to illustrate the solution procedure:

$$\rho\frac{\partial Y_i}{\partial \tau} = \rho\frac{\chi}{2}\frac{\partial^2 Y_i}{\partial Z^2} + \dot{\omega}_i, \tag{1a}$$

$$\rho\frac{\partial T}{\partial \tau} = \rho\frac{\chi}{2C_p}\left(\frac{\partial^2 T}{\partial Z^2} + \frac{1}{C_p}\frac{\partial C_p}{\partial Z}\frac{\partial T}{\partial Z}\right) - \sum_{i=1}^{n}\frac{h_i}{C_p}\dot{\omega}_i - \frac{1}{C_p}\dot{q}_R''' + \frac{1}{C_p}H + \frac{1}{C_p}\frac{\partial p}{\partial \tau}, \tag{1b}$$

where

$$\chi = 2D_Z\left(\frac{\partial Z}{\partial x_\alpha}\right)^2$$

is the instantaneous scalar dissipation rate which implicitly incorporates the influence of convection and diffusion normal to the surface of stoichiometric mixture. $\dot{q}_R'''$ is volumetric radiation rate and H is the enthalpy flux by mass diffusion. These two terms are not included in the simulation presented in this paper. The (physical) coordinate-free formulation of diffusion flamelets, as in the above equations, allows the use of arbitrarily complicated chemistry to obtain the mass fractions, Y_i, and relatively independent solution from the flow simulation if the parameter χ is given. The steady state results are compared in this paper, implying the exclusion of near extinction phenomena.

The flamelet equations take a more complicated form when differential diffusion effects are allowed[24]. The present project focuses on the unity Lewis number models.

The Newton-Raphson relaxation method is used to solve the two-point boundary value problems. To allow for the use of the matrix solver for "block diagonal" systems, Eqs. (1) are first transformed into a set of first order differential equations, and then approximated by finite-difference equations on a grid or mesh of points that spans $Z = 0$ to 1. As a typical example, the equation

$$\frac{d^2Y}{dZ^2} = g(Y,Z)$$

will be replaced by

$$\frac{dY}{dZ} = W$$

and

$$\frac{dW}{dZ} = g(Y,Z),$$

or, in discrete form,

$$E_{1,k} \equiv Y_k - Y_{k-1} - (Z_k - Z_{k-1})\cdot\frac{1}{2}(W_k + W_{k-1}) = 0,$$

$$E_{2,k} \equiv W_k - W_{k-1} - (Z_k - Z_{k-1})\cdot g\left(\frac{1}{2}(Y_k + Y_{k-1}), \frac{1}{2}(Z_k + Z_{k-1})\right) = 0,$$

where $k \in [2, M]$ is the k^{th} grid point. For a chemical system with N species on a mesh of M points, we then have $2(N+1)\times M$ coupled equations for a vector $\mathbf{S} = Y_{1,1}, \cdots, Y_{N,1}, T_1, W_{1,1}, \cdots, W_{N+1,1}, \cdots, Y_{1,M}, \cdots, Y_{N,M}, T_M, W_{1,M}, \cdots, W_{N+1,M}$. To solve the equations, a sequence of gradually improved solutions, $\mathbf{S}^{n+1}$, is formed from the previous solution $\mathbf{S}^n$ using Newton-Raphson's method:

$$J^n\left(\mathbf{S}^{n+1} - \mathbf{S}^n\right) = -\mathbf{E}(\mathbf{S}^n), \tag{2}$$

where $J^n \equiv \partial\mathbf{E}/\partial\mathbf{S}$ is the Jacobian matrix with dimension of $2(N+1)M \times 2(N+1)M$. Since $2(N+1)M$ can easily be several thousands, a straightforward matrix inversion in Eq. (7) is not feasible. A solver[25] which takes advantage of the special "block diagonal" matrix form of the equations, is adopted here.

The initial guess for $\mathbf{S}^0$ must be chosen to guarantee a convergent solution for the relaxation method. In the present work, the test problems for chemical reactions use a flame sheet to start the iterative procedure, wherein the fuel and the oxidizer are assumed to obey a single overall irreversible reaction of the type

$$\nu_F F + \nu_o O \rightarrow \nu_p P,$$

with or without an inert gas (N). In the limit of infinitely fast reactions, a flame sheet is formed between the fuel and the oxidizer streams such that fuel and

oxidizer cannot co-exist. Hence, on the fuel side of the flame ($Z \geq Z_{st}$), we have

$$T = T_2(1-Z) + T_1 Z + \frac{Q}{c_p} \cdot (Y_{F,1} Z - Y_F), \quad (1)$$

$$Y_F = Y_{F,1} Z + Y_{O,2} \frac{M_F \nu_F}{M_O \nu_O} (Z-1), \quad (2)$$

$$Y_O = 0, \quad (3)$$

$$Y_P = \frac{M_P \nu_P}{M_F \nu_F} (Y_{F,1} Z - Y_F), \quad (4)$$

and

$$Y_N = Y_{N,2}(1-Z) + Y_{N,1} Z. \quad (5)$$

On the oxidizer side, ($Z < Z_{st}$), we have

$$T = T_2(1-Z) + T_1 Z + \frac{Q}{c_p} \cdot Y_{F,1} Z, \quad (6)$$

$$Y_F = 0, \quad (7)$$

$$Y_O = Y_{O,2}(1-Z) - Y_{F,1} \frac{M_o \nu_o}{M_F \nu_F} Z, \quad (8)$$

$$Y_P = \frac{M_P \nu_P}{M_F \nu_F} Y_{F,1} Z, \quad (9)$$

and

$$Y_N = Y_{N,2}(1-Z) + Y_{N,1} Z. \quad (10)$$

Once the flame sheet starting estimate is obtained, we solve the full set of governing equations in a two-step procedure. We first determine a solution to the species equations (1(a)) based on the flame sheet temperature profile. This fixed temperature solution is then used as input to the full thermochemistry equations (Eqs. 1) in which the energy equation is solved along with the species equations. This procedure helps to reduce convergence difficulties and total CPU time. It has proved to be efficient in the counter-flow calculations[26]. It is also noted that a uniform mesh is sufficient for the convergence as the equations of species and temperature behave nicely in the mixture-fraction space.

6 Solution of the LES Equations

A finite-difference approach is employed to discretize the above equations. All discrete quantities are therefore assumed to be pointwise in nature. This choice is motivated by the relative ease of formal extension to higher-order accuracy.

6.1 Differencing Schemes

The difference schemes employed to solve the LES equations are compact (or Padé-type) for the spatial derivatives and the classical fourth-order Runge-Kutta for time integration. In compact-difference schemes, the derivative of a scalar quantity, ϕ say, is obtained in the uniformly discretized transformed plane (ξ, η, ζ) by solving the formula

$$\Gamma \phi'_{i-1} + \phi'_i + \Gamma \phi_{i+1} = b \frac{\phi_{i+2} - \phi_{i-2}}{4} + a \frac{\phi_{i+1} - \phi_{i-1}}{2} \quad (11)$$

where Γ, a and b determine the spatial properties of the algorithm. In this paper, the primary focus is on the fourth-order compact scheme, denoted $C4$, for which $\Gamma = \frac{1}{4}, a = \frac{3}{2}, b = 0$ and on the sixth-order scheme, $C6$, with $\Gamma = \frac{1}{3}, a = \frac{14}{9}, b = \frac{1}{9}$. Note that when Γ is non-zero, a tridiagonal system needs to be solved.

The three-point stencil of $C4$ necessitates special formulas at the end points 1 and IL. $C6$ requires special treatment at points 2 and $IL-1$ as well. At each of these points, higher-order one-sided formulas are utilized which retain the tridiagonal form of the equation set. At point 1 for example, the derivatives ϕ' are obtained from an equation of the form

$$\phi'_1 + \Gamma_1 \phi'_2 = \sum_{i=1}^{N} a_i \phi_i,$$

where N is the chosen order of accuracy. The coefficients in these formulas may be obtained from various sources in the literature, and have been collectively reproduced in Ref. 27.

The derivatives of the inviscid fluxes are obtained by first forming these fluxes at the nodes and subsequently differentiating each component with the above formulas. In order to reduce the error on stretched meshes, the required metrics are computed with the same scheme as employed for the fluxes. To form the terms containing the molecular viscosity and thermal or species diffusivity, the primitive variables are first differentiated and properly combined with the transport coefficients to form the requisite combinations of first derivative terms. These gradients are then differentiated again with the same difference scheme. Although this approach may not provide sufficient resistance to odd-even decoupling, no difficulty has been noted so far in this and other efforts since the filtering

approach described below guarantees the suppression of high-frequency modes.

The physical boundary conditions are applied after each update of the interior solution vector. These conditions include Dirichlet (no-slip) and Neumann (*e.g.*, extrapolation and symmetry) conditions.

6.2 Filtering scheme

Centered schemes such as those described above are susceptible to exponential growth of numerical instabilities, introduced most prominently by mesh non-uniformity, boundary condition implementation and capture of non-linear phenomena. The filtering procedure forms an important component of the present approach since its function is to stabilize the computations under these non-ideal conditions.

The filter is applied in a post-processing manner to the solution vector after the update at each time step– the time integration method is described below. Denoting a typical component of the solution vector by ϕ, filtered values $\widehat{\phi}$ satisfy

$$\alpha_f \widehat{\phi}_{i-1} + \widehat{\phi}_i + \alpha_f \widehat{\phi}_{i-1} = \sum_{n=0}^{N} \frac{a_n}{2} \left(\phi_{i+n} + \phi_{i-n}\right) \quad (12)$$

For multi-dimensional problems, the filter is applied sequentially in each of the three directions. This equation, with proper choice of coefficients, provides a $2N^{\text{th}}$-order formula on a $2N+1$ point stencil. The $N+1$ coefficients, $a_0, a_1 ..., a_N$, are derived in terms of α_f with Taylor- and Fourier-series analyses and are listed in [27]. Thus Eqn. 14 can be written as

$$\alpha_f \phi_{i-1} + \widehat{\phi}_i + \alpha_f \widehat{\phi}_{i-1} = f_{2N}\left(\alpha_f, \phi_{i-N}, ..., \phi_{i+N}\right),$$

where the right hand side is known once α_f and the order of accuracy, $2N$, are chosen. On uniform meshes, the resulting filters are non-dispersive. They do not amplify any waves and they preserve constant functions and completely eliminate the odd-even mode. Since α_f is a free parameter, an explicit filter i.e., one that does not require the solution of a tridiagonal matrix, can be easily extracted by setting $\alpha_f = 0$. The primary constraint on α_f is that it must satisfy the inequality $-0.5 < \alpha_f < 0.5$. In this range, higher values of α_f correspond to a less dissipative filter. At $\alpha_f = 0.5$, Eqn. 14 reduces to an identity and there is no filtering effect. Detailed spectral responses of these filters may be found in Refs. 28 and 27.

Computations on a range of 2-D and 3-D problems suggest that on meshes of reasonable quality, a value $0.3 \leq \alpha_f < 0.5$ is appropriate. Only in cases where the mesh is of extremely poor quality, if it contains metric discontinuities for example, will a lower value of $\alpha_f \sim 0.1$ be required. The impact of filtering on the fully discretized 1-D advection equation with periodic end conditions has been examined in Ref. 28.

The relatively large stencil of high-order filters requires special formulations at several points near the boundaries. For instance, the 10th-order interior filter requires an 11-point stencil and thus can not be applied at the "near-boundary" points 1, 2...5 and correspondingly at $IL-4, ...IL$, where it protrudes the boundary. The values at points 1 and IL are specified explicitly through the boundary conditions and are not filtered. At the remaining near-boundary points, two approaches have been noted in the literature. In Ref. 11, it was suggested that lower-order centered formulas be applied near the boundaries with appropriate adjustment (or optimization) of the value of α_f. This approach is based on the observation (see Ref. 29) that, for any given order of accuracy, as values of α_f approach 0.5, the dissipative effect of the filter is muted. The second method, introduced in Ref. 30 employs higher-order one-sided formulas. For the problems of present interest, either approach may be employed. Due to its simplicity, all computations reported in this work utilize the first approach.

6.3 Time Integration

The equations are integrated in time with the classical fourth-order four-stage Runge-Kutta method. With R denoting the residual, the governing equation is:

$$\frac{\partial U}{\partial t} = R = -J\left(\frac{\partial\left(F-F_v\right)}{\partial \xi} + \frac{\partial\left(G-G_v\right)}{\partial \eta} + \frac{\partial\left(H-H_v\right)}{\partial \zeta}\right) - S$$

The classical four-stage method integrates from time t_0 (step n) to $t_0 + \Delta t$ (step $n+1$) through the operations

$$k_0 = \Delta t R\left(U_0\right) \quad k_1 = \Delta t R\left(U_1\right)$$
$$k_2 = \Delta t R\left(U_2\right) \quad k_3 = \Delta t R\left(U_3\right)$$

$$U^{n+1} = U^n + \frac{1}{6}(k_0 + 2k_1 + 2k_2 + 2k_3)$$

where $U_0 = U(x, y, z, t_0), U_1 = \frac{k_0}{2}, U_2 = U_1 + \frac{k_1}{2}, U_3 = U_2 + k_2$. The scheme is implemented in the low-storage form described in Ref. 31, requiring 3 levels of storage for each variable.

7 Results and Discussion

7.1 Flamelet Calculations

The results for methane/air combustion using the flamelet model is discussed in this subsection to illustrate the usefulness of the procedure. Note that the LES equations were not solved and the results in this subsection are based entirely on equations 1 through 12. Therefore, the mixture fraction dissipation rate χ has to be specified independent of the flow equations. The results for the combined flamelet/LES calculations are presented in a later section. Results for hydrogen/air, propane/air, and Jet-A/air are also presented but can be explained along the same lines as those for methane/air. Several cases are reported in this paper using different models for the dissipation rate χ. A few cases were analyzed for constant χ values while, in other cases, χ was modeled as

$$\chi = \frac{a_s}{\pi} \exp\left\{-2\left(\text{erf}\, c^{-1}(2Z)\right)^2\right\},$$

following Peters[19], and a_s values of 5, 10, 50, 100, 300, and 600 used to study the sensitivity of species distribution. Above, erf c^{-1} is the inverse complimentary error function. Most of the cases in this section use stoichiometric mixture fraction values of $Z_{st} = 0.055$ and 1/3.

The results in figures 1(a) through 1(f) were obtained with the kinetic model of Bushe et al [20]. Figure 1(a) shows the species distribution as a function of Z for $\chi = 1$, $Z_{st} = 1/3$, which should be contrasted with Fig. 1(b), which uses Z-dependent χ with $a_s = 300\ s^{-1}$. The solid lines show the fast chemistry limit while the other lines are for finite chemistry. The dashed lines in Fig. 1 (a) are for fixed temperature (i.e., at the fast chemistry limit) whereas the dotted lines were finite chemistry results in which the energy equation was solved along with the species equations. The difference between these two results does not appear to be significant; hence the energy equation was not included in the calculation of the mass fractions for Mechanism 2 and the Full Mechanism. Relative to the fast chemistry values, larger product mass fractions can be observed for $\chi = 1$ than for $a_s = 300\ \text{s}^{-1}$. Including the energy equation has a negligible effect on the finite chemistry results for Y_p, Y_{O_2}, Y_{CH_4}, and Y_i. (Y_i is the mass fraction of the intermediate product in the mechanism of Bushe et al.)

Also using the model of Bushe et al., Figs. 1(c) through 1(e) show the effect of a_s for $a_s = 50, 300$, and 600, with $Z_{st} = 0.055$. Decreasing Y_p values with increasing a_s is evident. For the same Z, increasing a_s also shows increasing Y_{CH_4} relative to the fast limit results, which is consistent the decreasing Y_p values under the same conditions. Similar results can be seen for Y_{O_2} for $Z > Z_{st}$. Increasing a_s implies increasing strain rates and hence decreasing combustion activity. Increasing a_s also leads to decreasing maximum temperature (Fig. 1(f)). A comparison of some of these figures with the DNS results of Bushe et al. shows that the present flamelet calculations are correct.

Figs. 2(a) through 2(d) show the effects of χ values for the 4-step reduced mechanism of Chelliah et al. A constant χ value of 1 is used in Fig. 2(a) while Figs. 2(b) through 2(d) use $a_s = 10, 50, 300$, and 600 s^{-1}, respectively. The results employing constant χ and those in which this parameter depends on Z but with $a_s = 10$ are quite similar for all species shown (Figs. 2(a) and 2(c)). The results for $a_s = 50$ are also similar to these ones. At $a_s = 300$, some differences are apparent, relative to the results for the lower a_s values. For larger a_s values, the peaks of the finite rate species mass fractions have shifted toward the fuel side for Y_{CO}. The mass fractions of oxygen, Y_{O_2}, as well as Y_{CO} are smaller for $a_s = 10$ compared to $a_s = 300$, while Y_{H_2O}, Y_{CO_2}, and Y_{CH_4} are slightly larger (Figs. 2(b) and 2(c)), a trend that is more evident at $a_s = 600$ (Figs. 2(b) and 2(d)). For $a_s = 600$, only Y_{CO} shows the tendency for the peak mass fractions to shift to the right, relative to lower a_s values.

The shift in the location of the peak Y_{CO} and Y_{H_2O} mass fraction values from $Z = Z_{st}$ is evident in the figures. The inflection point in the Y_{O_2} distribution is also shifted toward the fuel side. On the other hand, the peak Y_{CO_2} occurs at approximately $Z = Z_{st}$ for all a_s values.

Figures 3(a) through 3(d) show the predictions by the detailed mechanism of the mass fractions for the same species as in Figs. 2(a) through 2(d), with a_s values of 10, 300, 600 and $\chi_s = 40$. For a_s=10, peak Y_{H_2O} lies in $Z < Z_{st}$ and of Y_{CO_2} in $Z > Z_{st}$. This behavior is reversed for a_s=300, 600. For the three cases, peak Y_{CO} is found in $Z > Z_{st}$. The magnitudes of these peaks for Y_{H_2O} and Y_{CO_2} decrease with a_s going from 10 to 600, as does the gradient $\left|\frac{dY_i}{dZ}\right|$ for these two species. The peak of Y_{CO} increases with a_s. The magnitude of Y_{CH_4} appears to decrease with a_s, consistent with the results obtained from the reduced models of Bushe et al. The tendency for the oxygen mass fraction to build up relative to the fast limit distribution also increases with increasing a_s. As Fig 3(d) shows, the results for $\chi = 40$ is indistinguishable from that for $a_s = 300$, except in the vicinity of the intersection of the curves for Y_{CO_2} and Y_{O_2} where $\frac{dY_{CO_2}}{dZ}$ is slightly larger for $a_s = 300$. Note that χ_s is the value of the dissipation rate evaluated at $Z = Z_{st}$. Figures 3(e) and 3(f) also support the closeness of the results for the two cases. In spite of the differences in the initial guess values (i.e., the fast limit results), the converged finite rate results are identical.

In Figs 4(a) and 4(b), the predictions by the three kinetics mechanisms are compared for $a_s = 10$ and 300, respectively. In the figures, the solid lines are the results for the detailed mechanism of Peters, while the dashed lines are for the 4-step reduced mechanism of Peters and Kee (1987) and the dotted lines refer to the 2-step mechanism of Bushe et al. Note that Y_i refers to the mass fraction of the quantity $(\frac{4}{3}H_2 + \frac{2}{3}CO)$ and Y_p is the mass fraction of the product, $(\frac{2}{3}H_2O + \frac{1}{3}CO_2)$. This quantity is calculated directly in the model by Bushe et al. whereas it is modeled for the models by Peter and Peter and Kee:

$$Y_i = \frac{M_i}{2}\left(\frac{3}{4}\frac{Y_{H_2}}{M_{H_2}} + \frac{3}{2}\frac{Y_{CO_2}}{M_{CO_2}}\right)$$

For all species, and using the detailed mechanism as the reference, the 4-step mechanism is visibly more accurate than the 2-step mechanism, particularly for Y_p and when $a_s = 300$. Compared to the other species, agreement among the three mechanisms is particularly good for Y_{CH_4}; the three curves for this case are coincident at $a_s = 10$. The results for Propane (Fig. 5), Jet-A (Fig. 6), and Hydrogen (Fig. 7) can be interpreted in a similar fashion to the discussions above for Methane.

7.2 Flamelet-LES Calculation of Homogeneous Turbulence

Reacting turbulent flow in a homogeneous box was calculated in order to evaluate the flamelet-LES procedure presented in this paper. The turbulence Mach number, M_t is 0.3 while the turbulence Reynolds number is 250. The initial flow is one that is just relaxing from a solenoidal velocity, pseudosound field.[32] The initial scalar field is as in Mell et al. The segregation parameter, S_o, is 0.814 where a value of zero means totally mixed reactants and 1 implies that fuel and oxidant are unmixed. Thus, a partially-mixed condition is simulated. The grid for DNS is 128×128 and for LES is 32×32 and a global one-step reaction for methane is calculated:

$$F + rO \rightarrow (r+1)\,P$$

The Damkhöler number, Da, is 10, Zeldovich number, Ze, =5 and the heat release parameter, Ce, is unity. Values of 0.055 and 0.5 are used for the stoichiometric mixture fraction

$$Z_{st} = \frac{Y_{O_2}}{rY_{F+1} + Y_{O_2}}.$$

The following models for the distribution of the PDF of the mixture fraction $f(Z)$ were investigated:

1. $\beta-$ distribution for $f(Z)$ as a function of Z.
2. $f(Z) = 2\left[H(Z-0.25) - H(Z-0.75)\right]$, where H is the Heaviside step function.
3. A Gaussian distribution of $f(Z)$ as a function of Z.

Note that the χ that appears in the flamelet equations is the stoichiometric value, χ_{st}. However, only $\widetilde{\chi}$ is available (from the LES step). Therefore models were tested for χ_{st}, as follows:

a) Counterflow model

$$\widetilde{\chi}_{st} \approx \widetilde{\chi}\frac{\exp\left\{-2\left[\mathrm{erf}\,c^{-1}\left(2Z_{st}\right)\right]^2\right\}}{\int_0^1 \exp\left\{-2\left[\mathrm{erf}\,c^{-1}\left(2Z_{st}\right)\right]^2\right\} p(Z)\,dZ},$$

where Z_{st} at the initial time is calculated from the fast chemistry limit, as discussed earlier in this paper. Note that although Z changes with time, Z_{st} does not for a single-phase combustion.

b)

$$\widetilde{\chi}_{st} \approx \widetilde{\chi}$$

c)

$$\widetilde{\chi}_{st} \approx 3\widetilde{\chi}$$

Figure 8 compares the flamelet-LES and DNS calculations for the three models for $\widetilde{\chi}_{st}$. The scatterplot shows that the assumption $\widetilde{\chi}_{st} = \widetilde{\chi}$ gives the best agreement between the flamelet-LES procedure and DNS. The worst is the counterflow model, wherein the model produces higher values of the combustion product, Y_p. At intermediate values of Y_p, the DNS results appear to yield larger values compared to the model $\widetilde{\chi}_{st} = 3\widetilde{\chi}$. Note that a priori testing is shown in Figure 8 in the sense that the $\widetilde{\chi}$ values were taken from the DNS calculations. The same a priori testing is carried out in Figure 9 which compares the $f(Z)$ models in the calculation of the reaction rate $\overline{\dot{w}}$. Note that in this case, $\dot{w}$ is modeled as

$$\overline{\dot{w}} = \int\int \dot{w}\left(Da, Y_i, Z, \chi_s\right) f(Z)\, f(\chi_s)\, dZ d\chi_s,$$

so that the assumed distribution, $f(Z)$, directly affects $\overline{\dot{w}}$. The "no-model" procedure for $\dot{w}$ is

$$\overline{\dot{w}}_i = A\widetilde{T}^n \widetilde{Y}_o \widetilde{Y}_F \exp\left(-\frac{E}{R\widetilde{T}}\right).$$

On the average, the β-distribution assumption shows the best agreement for whole range of $\overline{\dot{w}}$. The Gaussian profile also gives acceptable mean results, although the spread is too wide. The flamelet-LES procedure tends to underpredict $\overline{\dot{w}}$ when the uniform (Heaviside) distribution is used for $f(Z)$, although it, too, gives an unacceptably large spread. The "no-model" case shows higher values compared to the DNS but the spread is excellent, giving the appearance of better results. The "no-model" procedure is expected to yield poorer results (larger values of $\overline{\dot{w}}$ compared to DNS) for strong heat release situations. In the present calculation, the adiabatic temperature is roughly 1.1 times the initial maximum temperature, instead of a typical value of around 5 or greater.

Finally, a posteriori tests have also been carried out by the author but these are reported elsewhere. Contour maps of the fuel mass fraction field are shown in Figure 10 for the flamelet-LES and DNS calculations. Good agreement is evident although the fineness of the DNS grid gives contours that are more "pleasing to the eye".

7.3 Flamelet-LES Calculation of Mixing Layers

The developed procedure has been applied to the calculation of a spatially-evolving mixing layer. The time-dependent perturbations from the classical Michaelke's stability analysis are used at the inflow for the fluctuating velocities whereas the initial velocity field is a hyperbolic tangent, as is the mixture fraction field. The Navier-Stokes characteristic boundary condition (NSCBC) procedure is used to at the far field and outflow. The fast limit is used for the initial distribution of fuel, oxidant, and temperature. The DNS grid is 375×99 whereas the LES grid is 188×49. The following parameters are also used: $M_c = 0.125, \mathrm{Re}_\delta = 720$ and $\frac{U_2}{U_1} = 0.5$. The momentum thickness θ of the mixing layer has been calculated by both the flamelet-LES model and DNS (Fig 11). In the figure, the results for $\mathrm{Re} = 720$ are shown. G3 implies the LES grid whereas G1 is the DNS grid. The abbreviation 'SMG' in the legend stands for the Smagorinsky model. Legends without this abbreviation imply the DNS results. Good agreement between the model and DNS is apparent, particularly for $\chi/\delta_w\,(0) \leq 50$. Note the superior performance of the flamelet-LES calculations over the DNS results when the latter uses the same grid as the former and $\chi/\delta_w\,(0) > 80$.

The mixing layer domain is divided into four zones, as shown in Figure 12. Figure 13 compares the DNS and flamelet-LES calculations for the product at $t = 80$. Qualitative agreement can be observed. A priori test results for the mean reaction rate are acceptable relative to the DNS results for $\widetilde{\chi}_{st} = \overline{\chi}$, whereas those for the counterflow model are not (Figure 14). The latter model tends to produce very low values relative to DNS. A priori and a posteriori test results are shown in Figure 15 for the product, with the a priori results

showing better agreement. Upstream history of the layer contributes to the a posteriori test and hence this test is more rigorous.

8 Conclusion

The flamelet model has advantages in terms of its ability to calculate highly complex chemical reactions. This paper reports on the performance of the model for diffusion flames when combined with the Large Eddy Simulation (LES) and assumed probability density functions for the mixture fraction and its dissipation rate. The flamelet equations are reduced to a set of first order ordinary differential equations and calculated very cheaply using Newton's iteration. The LES models support both the standard Smagorinsky and the dynamic approaches and are numerically calculated using the sixth-order compact diffusing and tenth-order filtering schemes. Time integration is done with the standard fourth-order Runge-Kutta procedure. The effects of three models for the probability density function of the mixture fraction are discussed. Also presented are various assumptions for the stoichiometric value of the mixture fraction dissipation rate and the effect on the combustion simulation results. The application of the developed procedures to the combustion of methane/air, propane/air, jet-A/air, and hydrogen/air are reported. In the case of methane, the performance for homogeneous turbulence and spatially-evolving mixing layers are also reported.

Acknowledgments

The basic high-order compact differencing and filtering code used to solve the LES equations in this study was developed by Dr. Miguel R. Visbal and Dr. Datta V. Gaitonde of the Air Vehicle Directorate of Wright-Patterson, AFB. The collaboration with these colleagues is gratefully acknowledged by the authors.

References

[1] Lilly, D.K., On the application of the eddy viscosity concept in the inertial subrange of turbulence. Manuscript 123, NCAR, Colorado, (1996).

[2] Deardorff, J.W. J. Fluid Mech. 41, pp. 453-480, (1970)

[3] Smagorinsky, J. In "Large Eddy Simulation of Complex Engineering and Geophysical Flows", B. Galperin and S. Orszag, Eds, Cambridge University press, pp. 2-36, (1993).

[4] Gao, F. and O'Brien, E. E., Phys. Fluids A, 5, pp. 1282-1284, (1993)

[5] Cook, A. W. and Riley, J.J., Phys. Fluids A, 6, pp. 2868-2870, (1994).

[6] Frankel, S.H., Adumitroaie, V., Madnia, C.K., and Givi, P. In "Engineering Applications of Large Eddy Simulations", Fluids Engineering Div., ASME, Vol. 162, pp. 81-101, (1993).

[7] Menon, S., McMurtry, P.A., and Kerstein, A., As in Ref 3 above.

[8] Smith, T.M . and Menon, S., AIAA 98-0242

[9] Cook, A. W. and Riley, J. J. Combustion and Flame 112:593, (1998).

[10] Chakravarthy, V.K. and Menon, S. Large eddy simulation of stationary premixed flames using a subgrid flamelet approach. In "Recent Advances in DNS and LES", (D. Knight and L. Sakell, Eds.), Kluwer Academic Publishers, pp. 85-98.

[11] Colucci, P.J., et al. Phys. Fluids 10, pp. 499-515 (1994).

[12] Garrick, S.C., Jaberi, F.A. and Givi, P., Large eddy simulation of scalar transport in turbulent jet flow. In "Recent Advances in DNS and LES", (D. Knight and L. Sakell, Eds.), Kluwer Academic Publishers, pp. 85-98.

[13] Peters, N., Laminar diffusion flamelet models in non-premixed turbulent combustion, *Prog. Energy Combust. Sci.*, Vol. **10,** p. 319-339 (1984).

[14] Cook, A.W. and Riley, J.J., Subgrid-scale modeling for turbulent reacting flows, Combustion and Flame, 112, pp: 593-606.

[15] Lele, S.K. Compact finite difference schemes with spectra-like resolution, J. Comp. Phys. 103, pp. 12-42.

[16] Visbal, M.R. and Gaitonde, D.V., very high-order spatially implicit schemes for computational acoustics on curvilinear meshes, Accepted by J. Acoustics, (2000).

[17] Ladeinde, F., Cai, X. and Sekar, B. Flamelet studies of reduced and detailed kinetic mechanisms for methane/air diffusion flames, paper 2000-GT-144, IGTI Congress and Exhibition, Munich, Germany.

[18] Williams, F.A, *Combustion Theory*, the Benjamin/Cummings Publishing Co., Menlo Park (1985).

[19] Peters, N., Four lectures on turbulent combustion, ERCOFTAC Summer School, September 15-19, 1997, Aachen, Germany.

[20] Bushe, W.K., Bilger, R.W. and Ruetsch, W.C., Incorporating realistic chemistry into direct numerical simulations of turbulent non-premixed combustion, *CTR Annual Research Briefs*, Stanford, p. 195 (1997).

[21] Peters, N. and Kee, R.J., *Combust. Flame,* 68, pp. 17-29 (1987).

[22] Chelliah, H.K., Seshadri, K. and Law, C.K., Reduced kinetic mechanisms for counterflow methane/Air diffusion flames, In "Reduced kinetic mechanisms for applications in combustion systems", *Lectures Notes in Physics, m 15,* Norbert Peters and Bernd Roggs, eds. Springer-Verlag., pp. 224-240 (1993).

[23] Peters, N., Flame calculations with reduced mechanisms - An outline, In "Reduced kinetic mechanisms for applications in combustion systems", *Lectures Notes in Physics, m 15,* Norbert Peters and Bernd Roggs, eds. Springer-Verlag., pp. 3-14 (1993).

[24] Pitsch, H. and Peters, N., A consistent flamelet formulation for non-premixed combustion considering differential diffusion effects, *Combust. Flame* 114, pp. 26-40 (1998).

[25] Press, W.H., Teukolsky, S.A., Vetterling, W.T., and Flannery, B.P., *Numerical Recipes in Fortran 77 (2nd ed.),* p. 757 (1992), Cambridge University Press.

[26] Keyes, D.E. and Smooke, M.D., Flame sheet starting estimates for counterflow diffusion flame problems, *J. Comput. Phys.* p. 267 (1987)

[27] D.V. Gaitonde and M.R. Visbal. High-order Schemes for Navier-Stokes Equations: Algorithm and Implementation into FDL3dI. Technical Report AFRL-VA-WP-TR-1998-3060, Air Force Research Laboratory, Wright-Patterson AFB, 1998.

[28] D. Gaitonde, J.S. Shang, and J.L. Young. Practical Aspects of High-order Accurate Finite-Volume Schemes for Electromagnetics. *AIAA Paper 97-0363*, Jan. 1997

[29] M.R. Visbal and D.V. Gaitonde. High-Order Accurate methods for Unsteady Vortical Flows on Curvilinear Meshes. *AIAA Paper 98-0131*, January 1998.

[30] D.V. Gaitonde and M.R. Visbal. Further Development of a Navier-Stokes Solution Procedure Based on Higher-Order Formulas. *AIAA Paper 99-0557*, January 1999.

[31] D.J. Fyfe. Economical Evaluation of Runge Kutta Formulae. *Math. Comput.*, 20:392-398, 1966

[32] F. Ladeinde, E.E. O'Brien, X. Cai., M. Liu, Advection by polytropic compressible turbulence, Phys. Fluids 48 (11) (1995) 2848-2857.

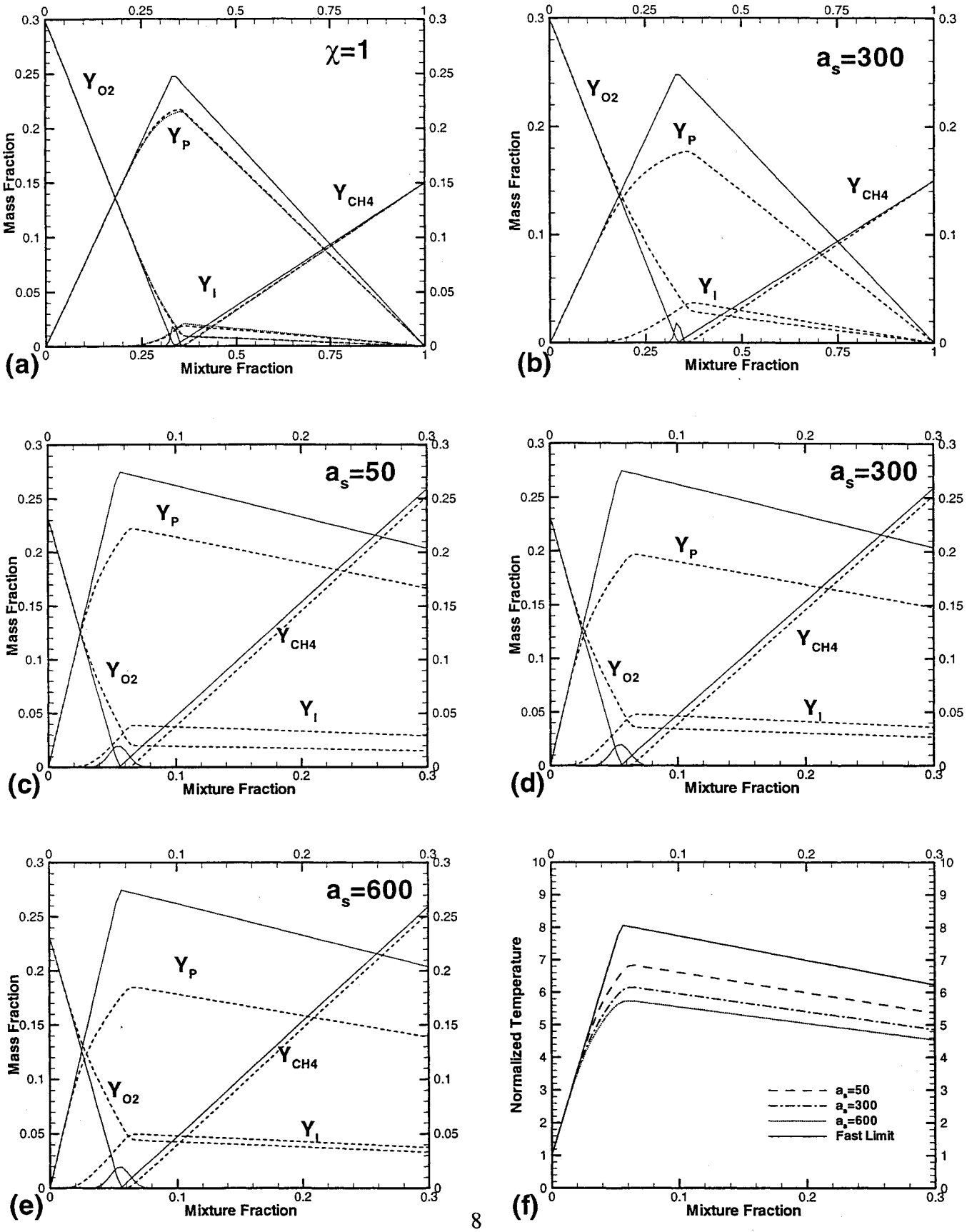

Figure 1. Flamelet results for methane: Mechanism 1.

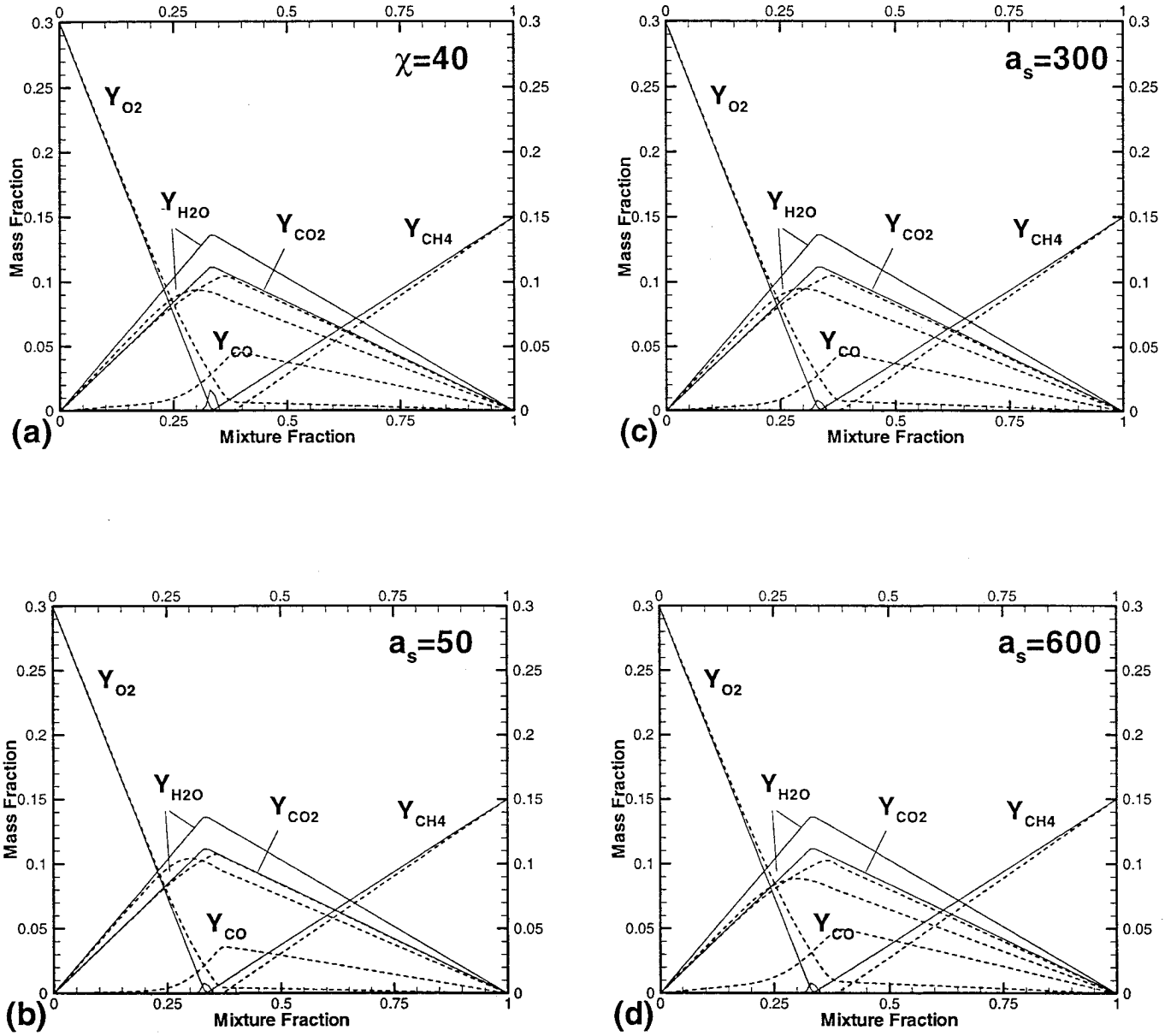

Figure 2. Flamelet results for methane: Mechanism 2.

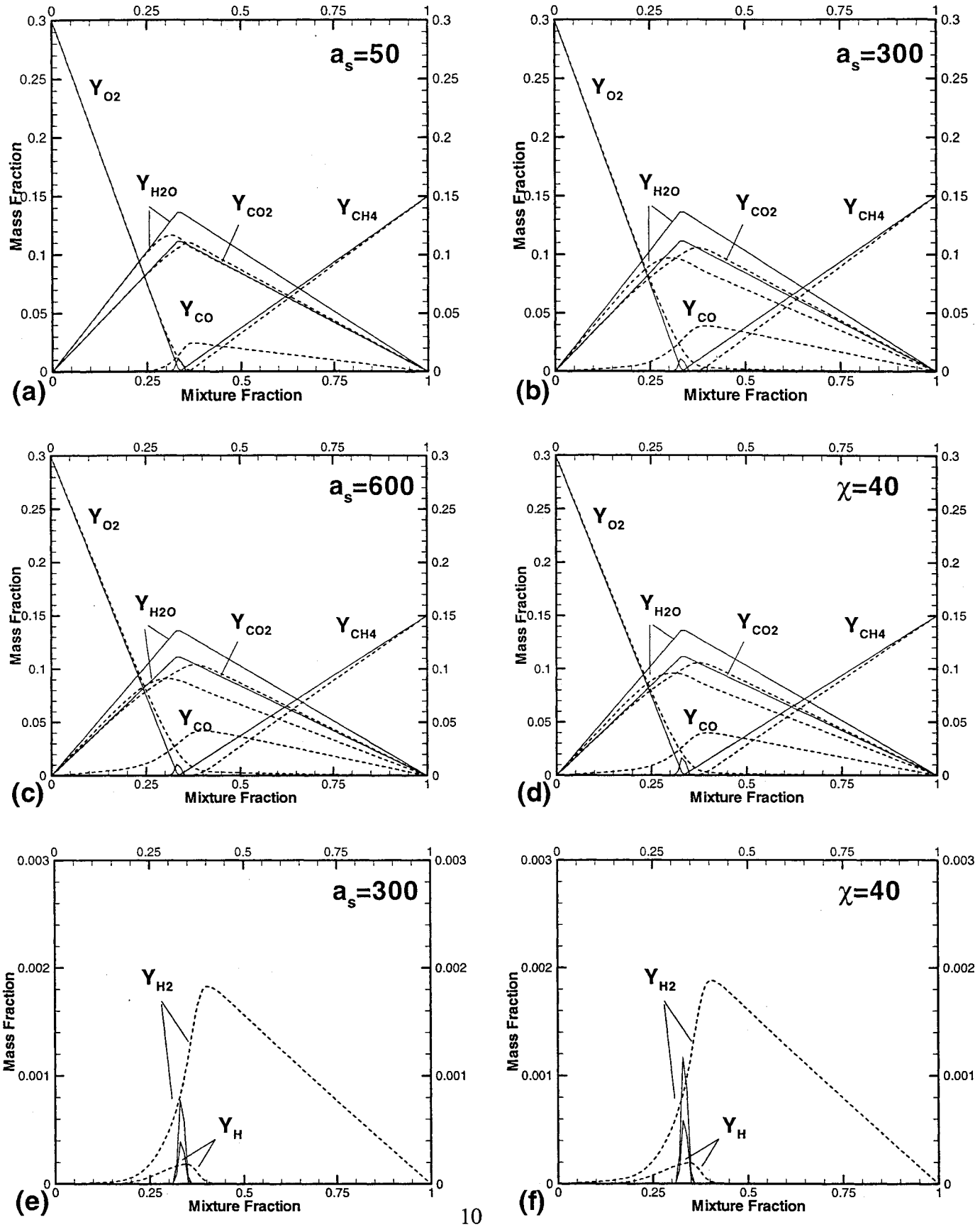

Figure 3. Flamelet results for methane: Mechanism 3.

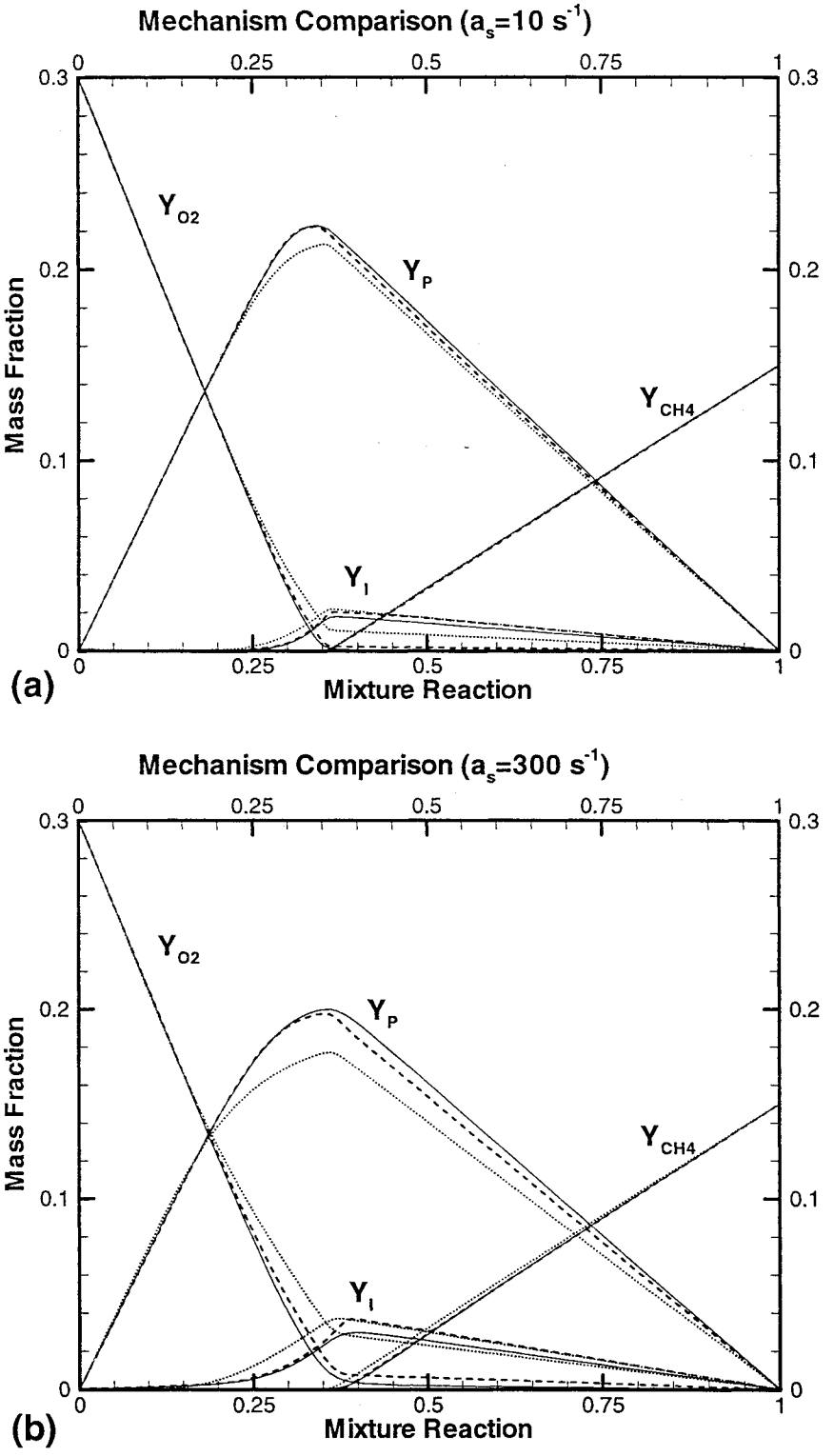

Figure 4 Mechanism Comparison. Solid Lines: Full Mechanism; Dashed Lines: Mechanism 2; Dotted Lines: Mechanism 1.

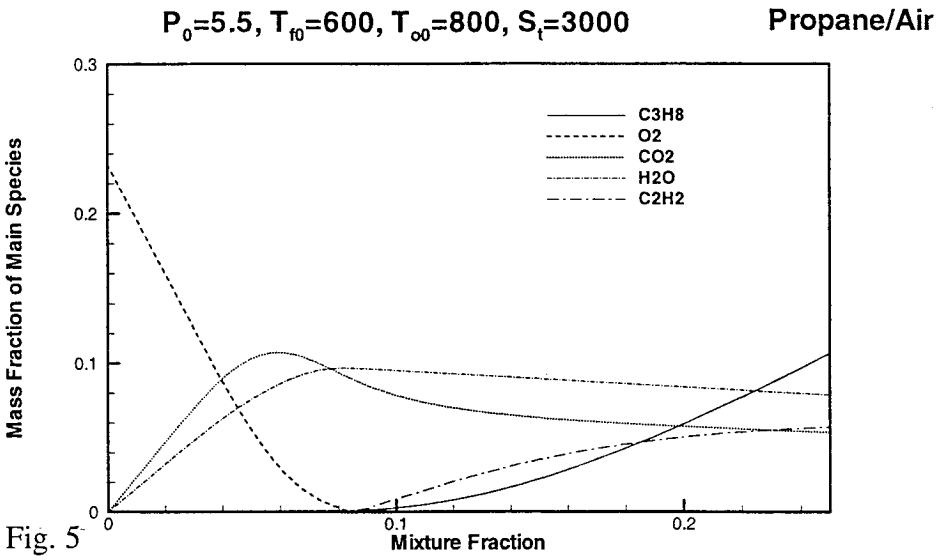

Fig. 5

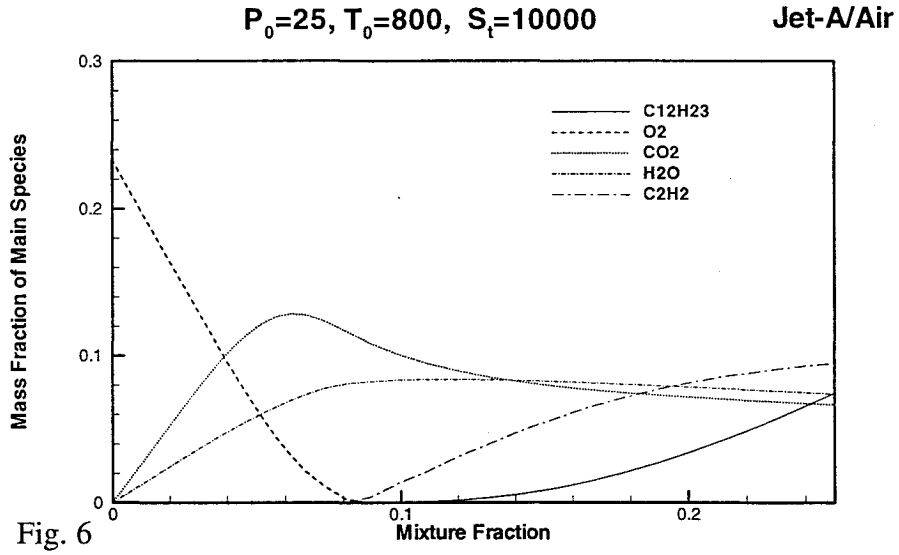

Fig. 6

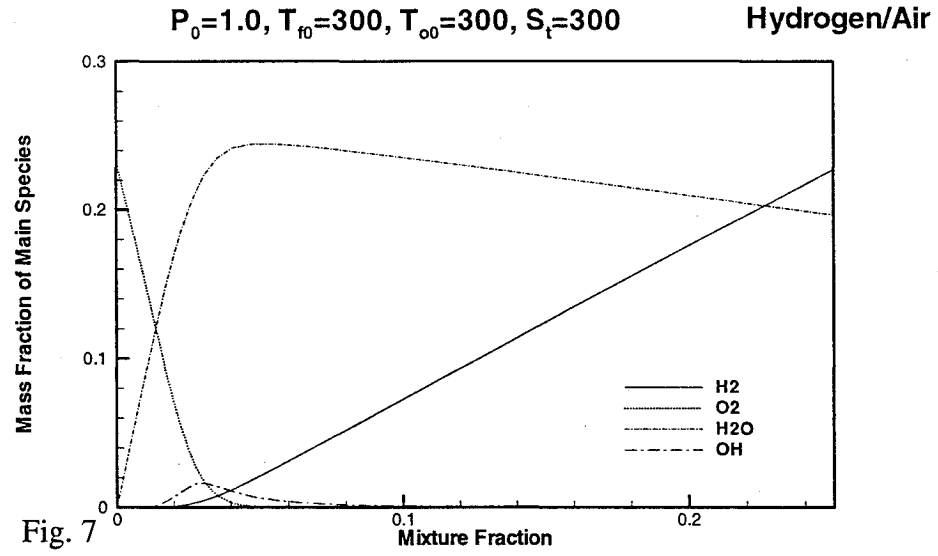

Fig. 7

Figure 5 through 7: Flamelet results for Propane, Jet-A, and Hydrogen, respectively.

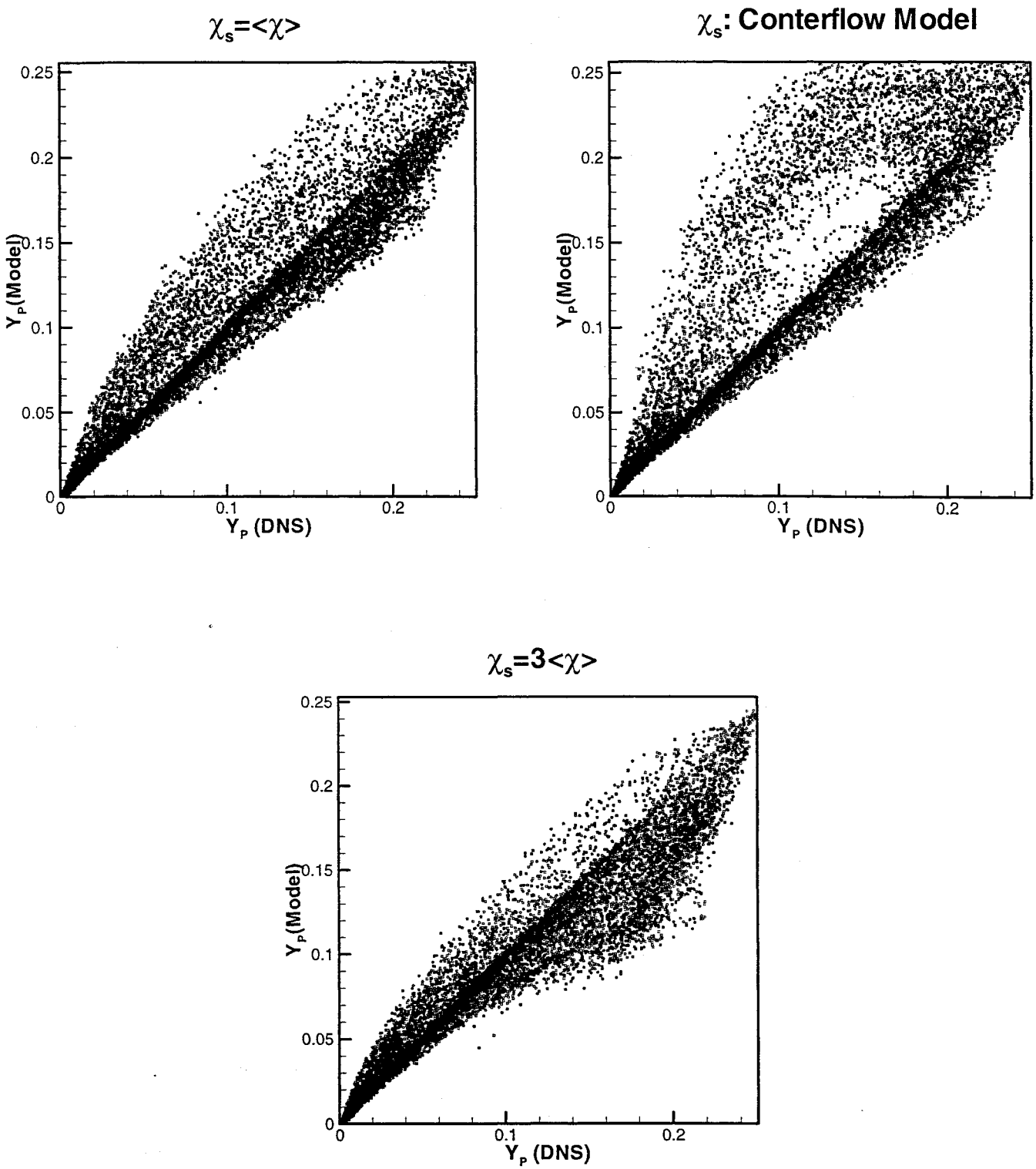

Figure 8. A Priori Test of Conditional Dissipation Model (Homogeneous Turbulence, Z_{st}=0.055)

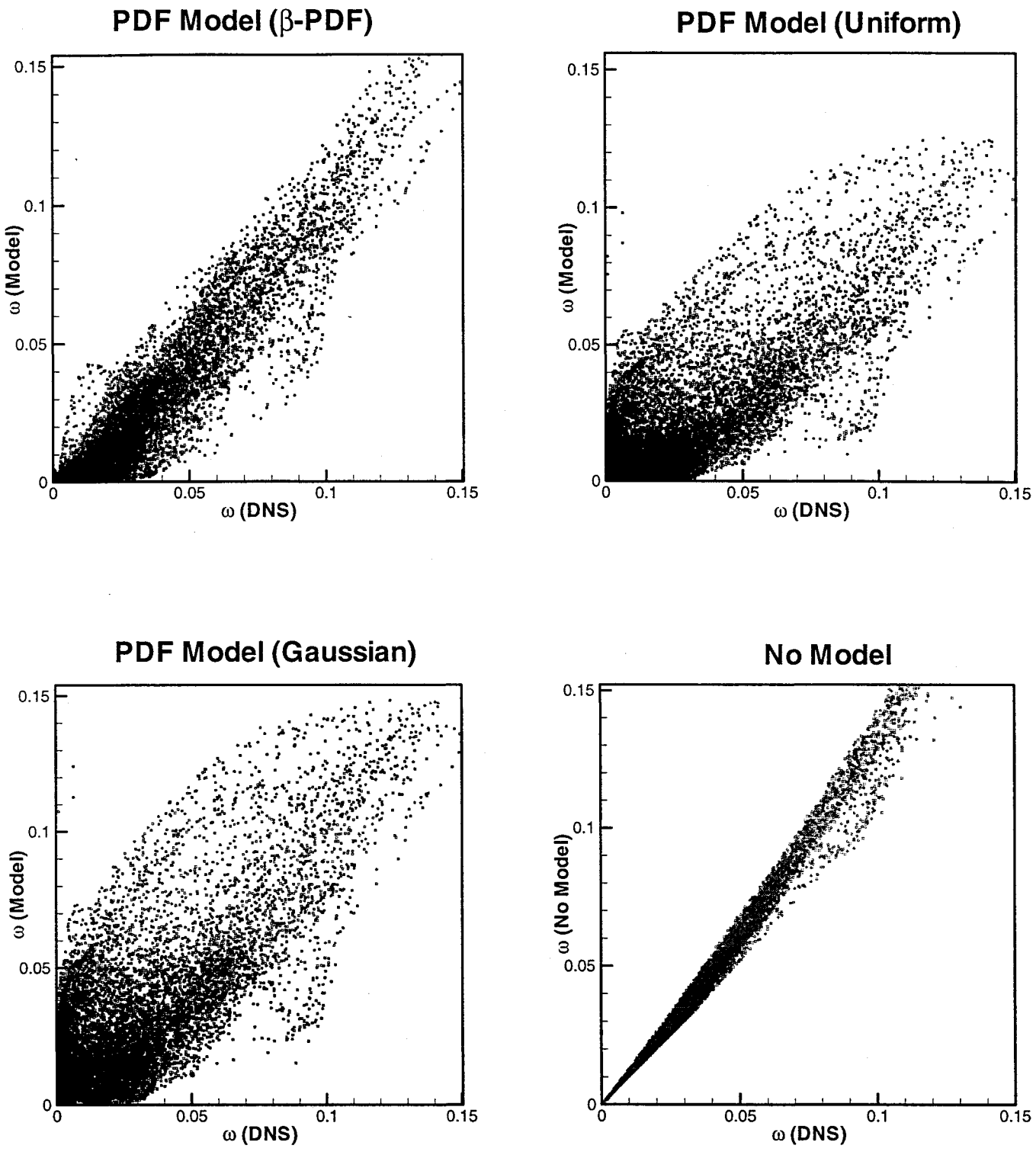

Figure 9. A Priori Test of PDF Form (Homogeneous Turbulence, Z_{st}=0.5)

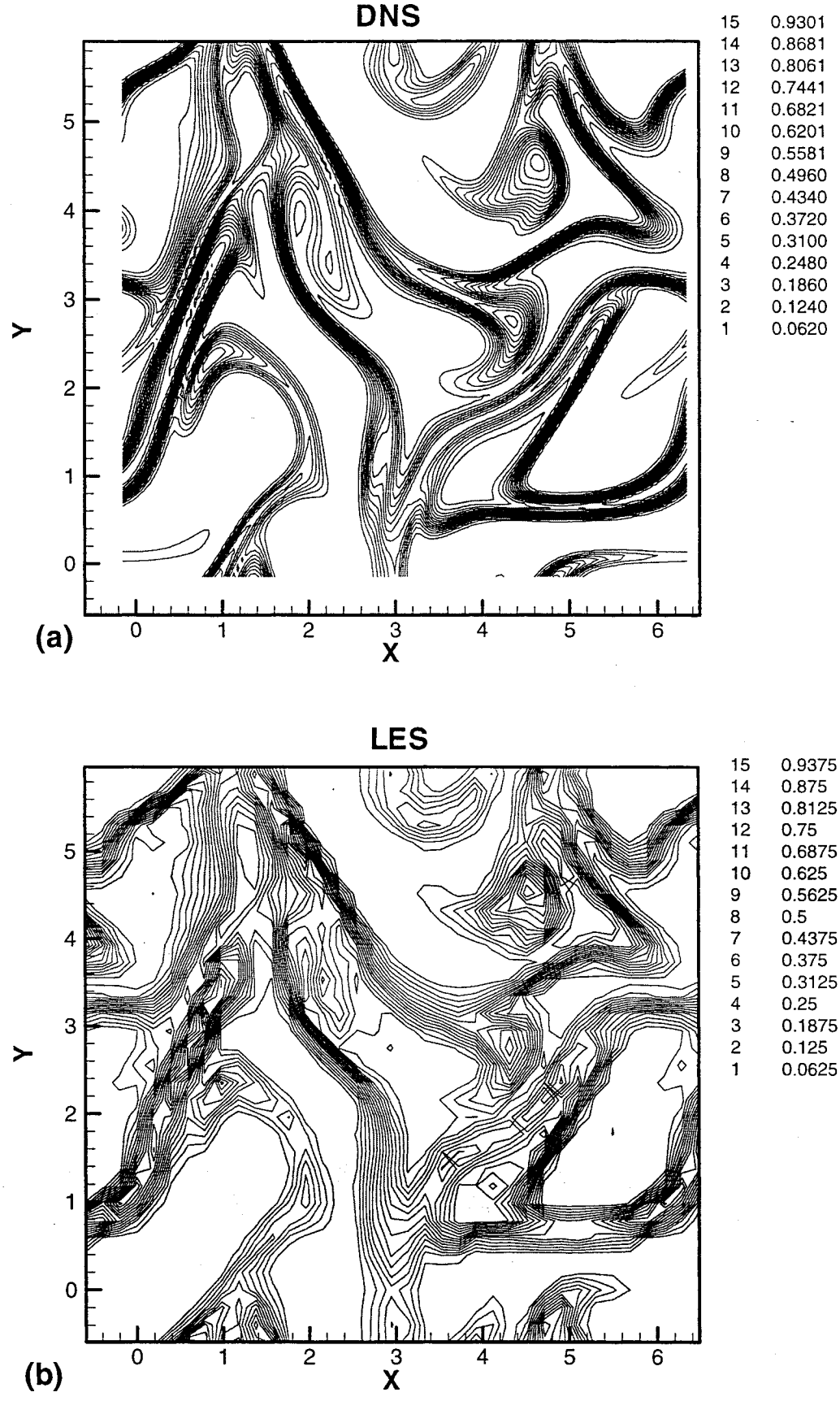

Figure 10. Contour maps of fuel distribution (Homogeneous Turbulence, Z_{st}=0.5): a) DNS; b) Flamelet-LES

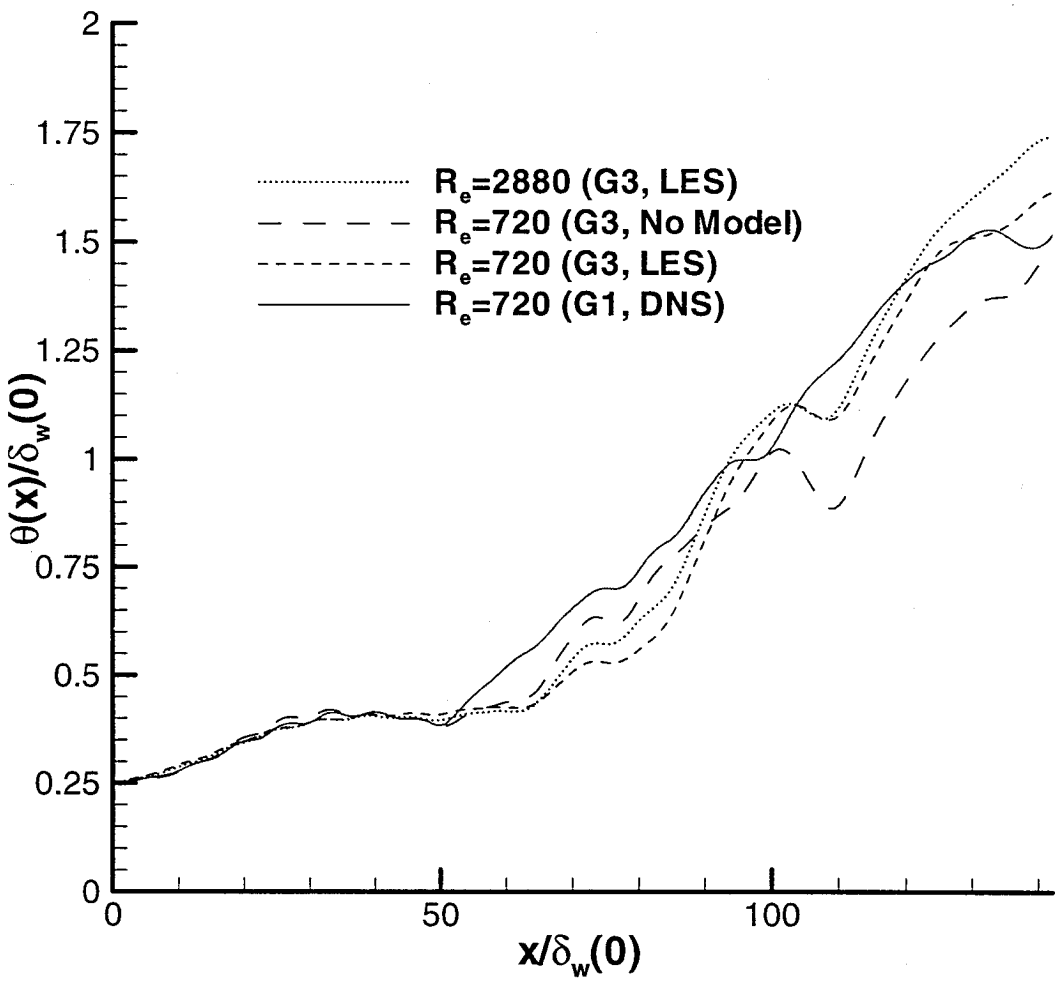

Figure 11. Comparison of moment thickness for DNS and Flamlet-LES calculations of spatially-developing mixing layer

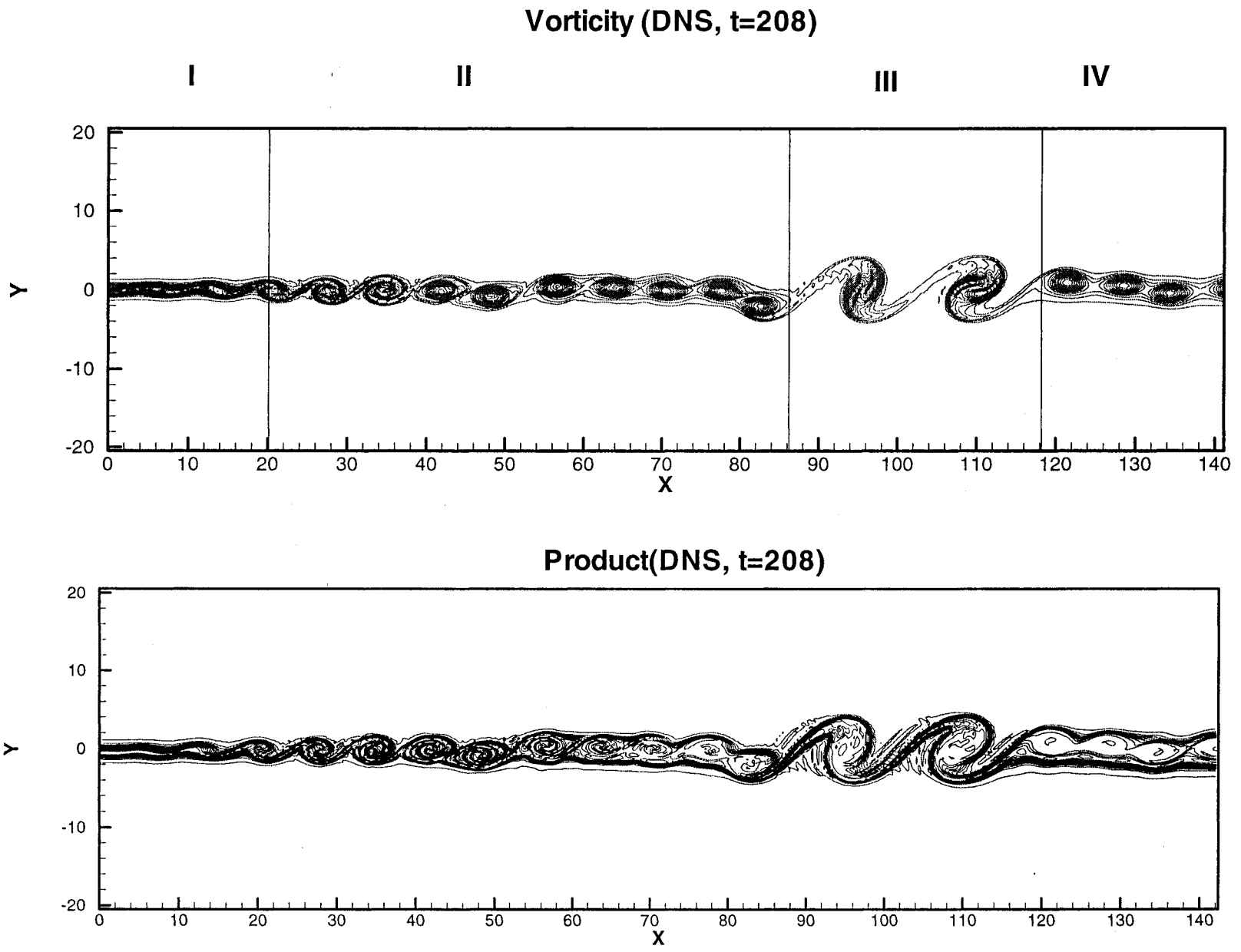

Figure 12. Samples of DNS results for methanecombustion in a spatially-developing mixing layer (The x-domain is partioned into four zones with different flow patterns).

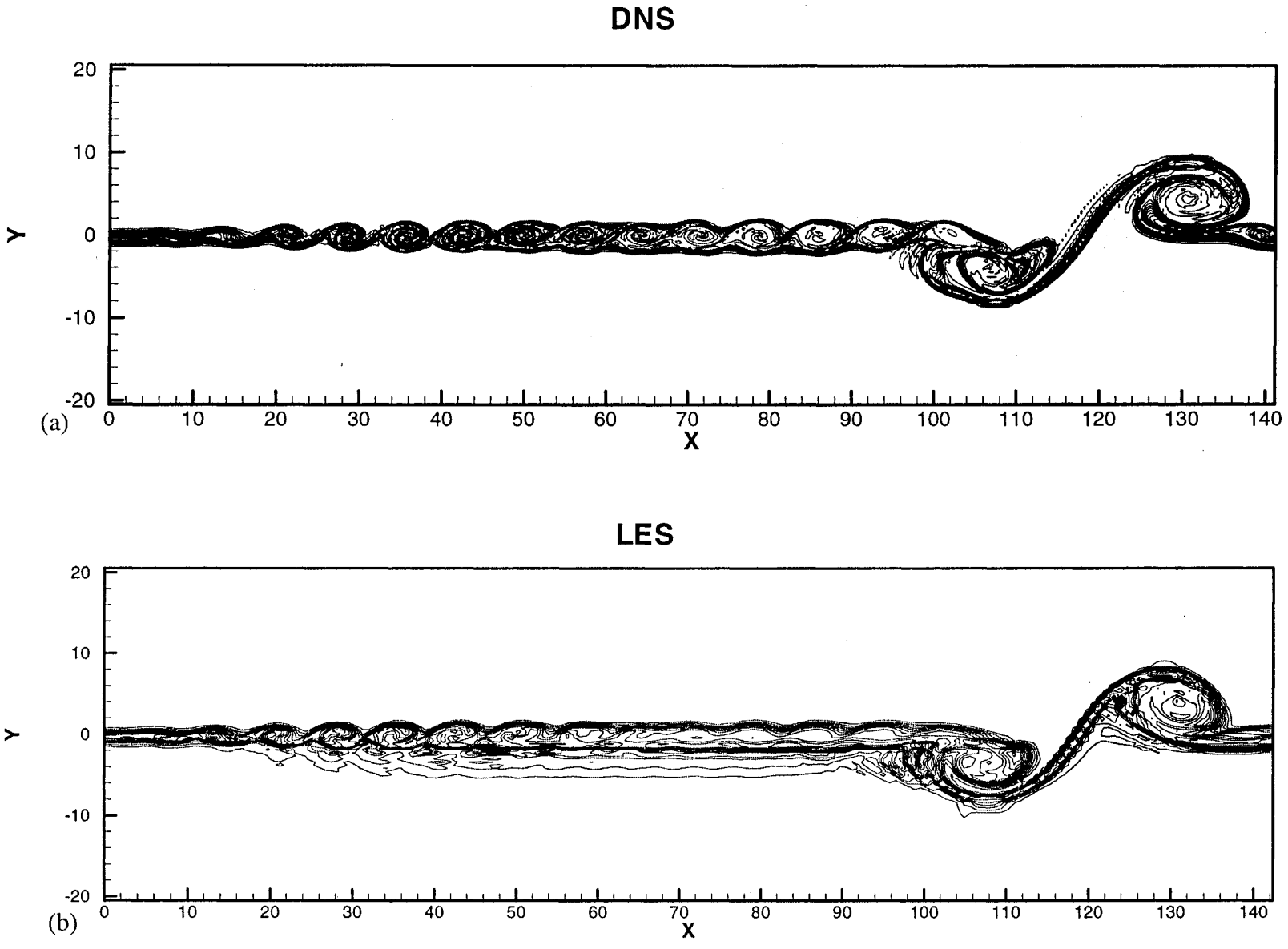

Figure 13. Contour maps of product distributions in a spatially-developing mixing layer (t=80): a) DNS; b) Flamelet-LES.

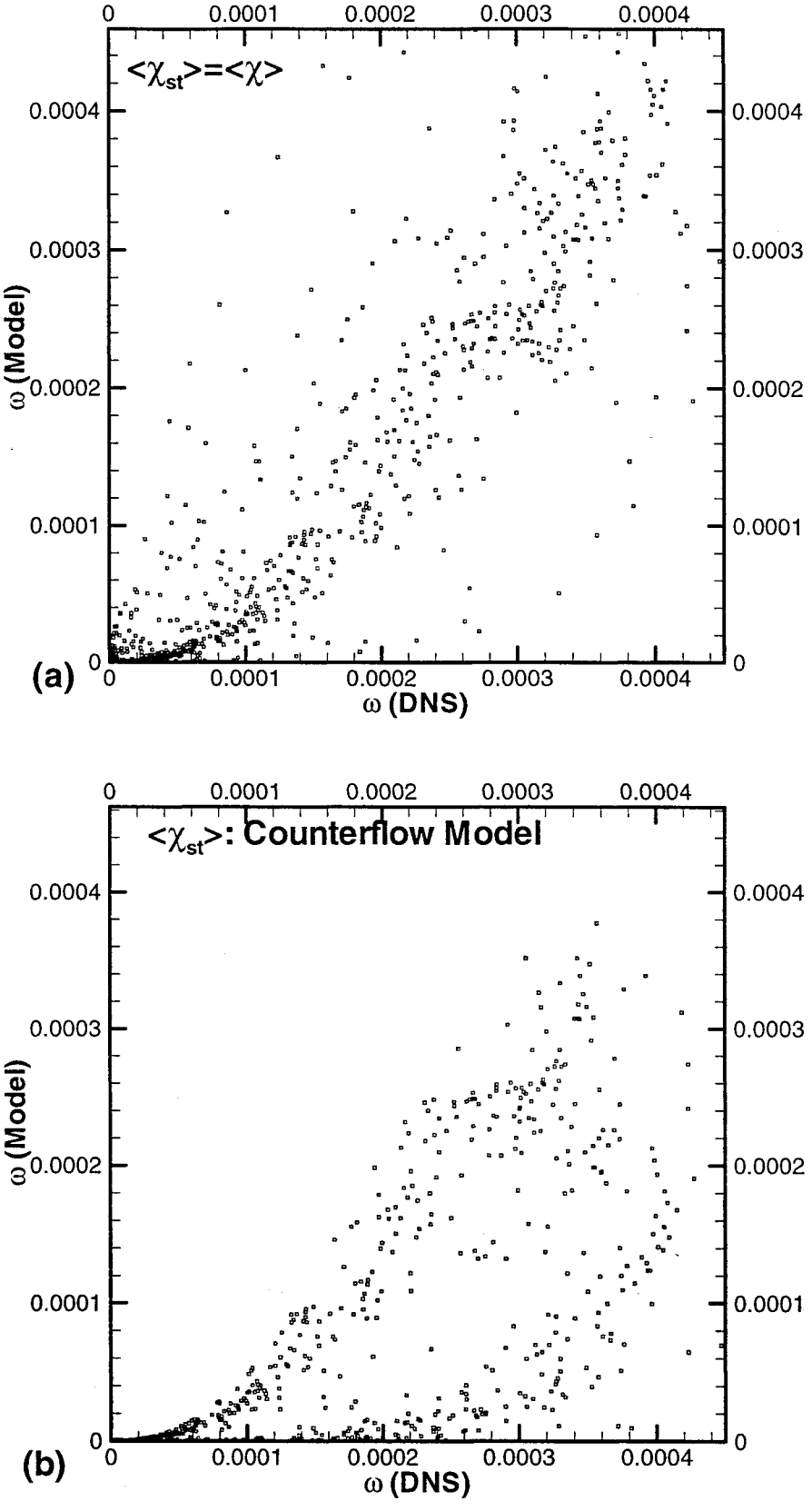

Figure 14. A Priori Test of Conditional Dissipation Rate (Zone IV of the Mixing Layer, Z_{st}=0.055, t=208).

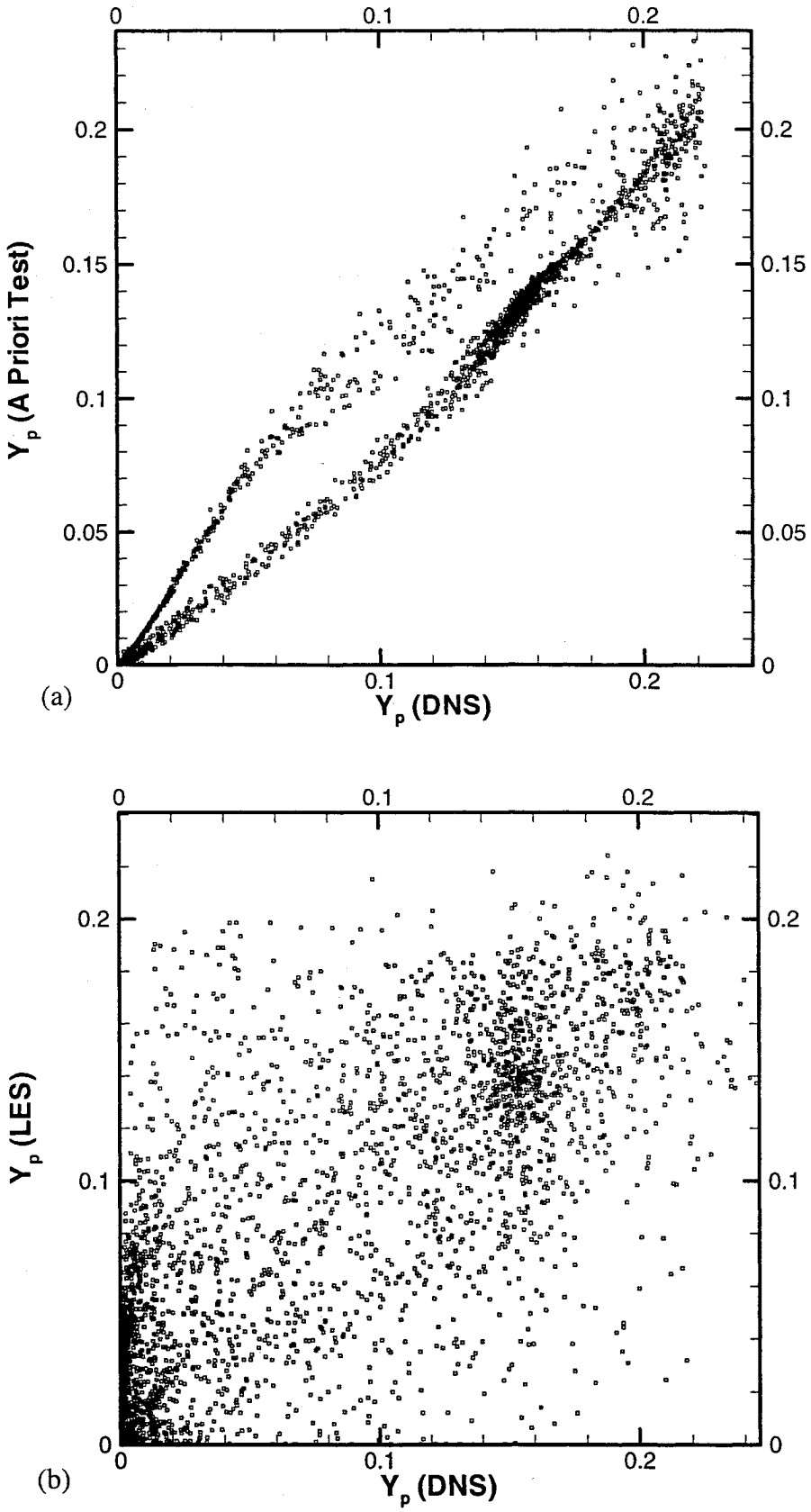

Figure 15. Comparison of product distributions in a spatially-developing mixing layer (Zone IV, Z_{st}=0.055, t=208): a) A Priori Test; b) A Posteriori Test.